NON-RIGID REGISTRATION OF CONTRAST-ENHANCED DYNAMIC MR MAMMOGRAPHY

TAN EK TSOON

NATIONAL UNIVERSITY OF SINGAPORE

2004

ACKNOWLEDGEMENTS

I will like to thank my supervisors for their tremendous help and advice. They have taught me so much, and have helped me at many junctures throughout my research in NUS for which I am extremely grateful. Many thanks to Associate Professor Ong Sim Heng, for his invaluable guidance in image processing and in all matters academic, especially in the writing of this thesis; Dr Yan Chye Hwang for his expertise in image registration and for always providing new ideas and directions in my research; and Associate Professor Wang Shih-Chang for lending his immense experience in MRM, time, patience, and for providing the added value to our work that brings it closer to becoming a feasible clinical application.

Also, I will like to thank many others who have provided the assistance when needed: Francis from the Vision and Image Processing laboratory for handling all the administrative matters; and Christopher and Lee Lian from the Functional Imaging Center in NUH for giving me a better appreciation of MRM. Thanks also to my research internship programme students Shaun, Xu Ce and Siang Koon for assisting me with various aspects of the project.

TABLE OF CONTENTS

SUMMARY

Contrast-enhanced dynamic MRI (CE-MRI) or MR mammography (MRM) is an alternative method to conventional X-ray mammography for non-invasive detection of breast cancer. It is superior in its 3-D tomography, excellent tissue resolution, and is free from ionizing radiation. A contrast agent (Gadolinium-DTPA) is injected to create an intensity increase in highly vascular regions that are indicative of malignant lesions. Analyzing the uptake rate of the contrast agent in a series of dynamic scans determines whether lesions are malignant or not. CE-MRI requires image registration to model the inevitable patient movement that occurs during the time needed to distinguish malignancy. Without image registration, motion artefacts corrupt the scans, making analysis of the uptake rate unreliable.

The current registration paradigm uses rigid registration to model global motion and multi-resolution non-rigid registration to model local motion. However, the optimization is slow and can lead to unreliable results. This thesis presents a new and intuitive contrast-enhancement model for normalized mutual information (NMI) non-rigid registration. It matches or surpasses traditional NMI registration in registration quality and it is also much faster. The proposed contrast enhancement model parameterizes NMI optimization, achieving speed and optimization efficiency. We also incorporate the clinically established 3 time-point (3TP) method into our registration technique to validate the assumptions of the model.

Comparisons are made on 42 sets of breast registrations – 20 are normal breasts and 22 are breasts with lesions (benign and malignant). The quantitative measurements of registration quality reveal that non-rigid registration surpasses rigid registration. Visual assessments from a clinical reader concur; registration produces images of at least equal visual quality as images without registration, and improves visual quality most of the time. We also show that the time required for the new registration scheme is approximately proportional to the image size.

A software package has been developed to register CE-MRI, and uses the 3TP method for analysis. This tool allows clinicians to reliably analyze the results of MRM registration. This software will be used in the National University Hospital of Singapore for clinical research.

LIST OF FIGURES

LIST OF TABLES

CHAPTER ONE

INTRODUCTION

Breast cancer is the most common type of cancer affecting women, and is the number two cause for cancer death in the world. In a general population study on Singapore from 1993-97, 3,574 breast cancer cases were diagnosed, and the incidence rate of breast cancer was one out of every four or five female cancers (22.8%) (Chia *et al.*, 2000). This rate was projected to double every 25 years. A follow-up study from 1998-99 revealed that the age-standardized incidence rate[1] had risen from 46.1 to 53.1 cases per 100,000 persons (Chia *et al.*, 2002). While the incidence rate in Singapore still lagged behind that in the West, nearly half of the affected women here were below 50 years of age and the rate for women between 40 to 50 years of age mirrored that in the West. The best way of fighting breast cancer is early detection. The conventional non-invasive method of breast cancer detection is using X-ray mammography, which is two-dimensional and poses a radiation risk.

Contrast-enhanced MRI (CE-MRI) has been proposed as an alternative method to conventional X-ray mammography for non-invasive detection of breast cancer. MRI is superior in its 3-D tomography, higher sensitivity to dense glandular tissue, and is radiation-free. When injected intravenously, the paramagnetic contrast-agent (Gadolinium-DTPA) increases the image intensity in regions of the breast parenchyma with higher vascularity. By taking a series of 3-D scans (one scan taken before the

[1] The rate of new cancers per 100,000 women per year over a specific time period adjusted for a reference age distribution; permits meaningful comparisons between differing national or regional cancer occurrence rates.

contrast agent is introduced), the uptake rate of the contrast agent may be used to identify whether tissue is likely to be malignant or benign.

However, CE-MRI mammography suffers from inevitable patient movement that creates blurring artefacts within each acquisition scan and motion artefacts between scans. Blurring artefacts can be reduced with improvements in MRI technology, but motion artefacts are inherent in serial repeated scans because patient motion is either physiological (e.g., respiration, cardiac motion) or involuntary (slight shifts in body position). Such motion is neither systematic nor predictable. The breast is also soft and deformable. Therefore to correct motion artefacts, an image registration technique that models both non-rigid motion and non-uniform increase in intensity is required. Image registration optimizes a cost function to align any two sets of scans; typically the pre-contrast scan is aligned against another post-contrast scan.

Registration usually requires the use of positional markers to align two images. However, in CE-MRI mammography, external markers cannot be used because the motion is non-rigid; internal markers also cannot be used because there are no distinct internal landmarks in breasts. Thus, a volume-registration approach has to be taken. Recently non-rigid registration methods favor the optimization of mutual information (MI) or the overlap-invariant normalized MI (NMI) as cost functions, as these can account for the non-uniform increase in intensity (Rueckert *et al.*, 1999; Hayton *et al.*, 1999). This approach has consistently shown visual and quantitative improvements, and has been verified using biomechanical models (Schnabel *et al.*, 2001, and 2003). However, several challenges remain unconquered. Firstly, the entropy calculations required in optimizing NMI are computationally exhaustive; secondly, NMI's high

propensity to enter local minima during optimization; thirdly, reduction in lesion volume (Tanner *et al.*, 2001) occurs due to non-rigid registration; finally, few references have been made to clinically verified methods of relating enhancement curves to malignancy.

The contributions in this work focus on applying a new contrast enhancement model that integrates NMI with the clinically established 3TP method (Degani *et al.*, 1997) to increase efficiency and improve generalization. We demonstrate that optimization of NMI may result in unnatural deformations regardless of regularization, which are the cause of the observed reduction in lesion volumes. We obtain a new cost function from the new model, which we show is faster and theoretically better than the current NMI registration paradigm. The results show improvements in registration quality, in quantified measurements and visual assessments from a clinical reader.

The ultimate objective of this project was to create image registration software customized for breast cancer research and detection using CE-MRI in the National University Hospital (NUH) in Singapore.

This thesis begins with a literature survey of background information and current medical image registration methods in Chapter 2. In the next chapter, the theory of the mathematical tools used in the non-rigid registration method is covered. Chapter 4 explains in detail how the registration scheme is implemented. Chapter 5 explains the model of contrast enhancement. The results and discussion are presented in Chapter 6, prior to conclusion.

CHAPTER TWO

BACKGROUND AND RELATED TOPICS

2.1 Breast cancer and mammography

Several large scale randomised clinical trials have shown that breast cancer screening with breast x-rays (mammography) can detect breast cancer much earlier than clinical palpation or breast self-examination, thus reducing mortality by about 30% in the screened population group. Prior to these trials, it had not been proven that any type of surgical, medical or radiation therapy improved breast cancer survival rates. Because breast cancer is the most common cancer in most developed nations, early detection through mass population screening has been both recommended and implemented in the form of national mammography-based breast screening programs in many countries.

With non-invasive methods of screening come the following advantages: (i) Early detection of breast cancer to lower mortality rates; and (ii) Accurate pre-operative localization of lesions to minimize the number of operations needed for complete surgical removal. Current non-invasive screening methods include using x-ray, ultrasonography and magnetic resonance imaging (MRI). X-ray is the established standard imaging modality for screening, and remains the only imaging method proven to reduce breast cancer mortality. About 5-10%[2] of women who undergo x-ray mammography have additional views and/or ultrasound of the breast.

[2] S.C. Wang, NUH DDR, personal communication, 2003.

X-ray mammography (i) has a high spatial resolution of about 50μm; (ii) has fairly high sensitivity and specificity[3] for breast (cancer) in fatty tissues[4]; and (iii) is relatively low in cost. It is useful in detecting radio-opaque micro-calcifications and lesions. Two-dimensional images are acquired, typically in the medio-lateral oblique and cranio-caudal views. Spatial correspondences of suspected abnormalities are established by matching the images from the two views. Figure 2.1 shows a mammogram taken from two views. Lesions and calcifications that appear to correspond are matched visually to deduce their locations in 3-D space. However, as x-rays are projective in nature, this spatial matching may be erroneous. X-ray also has low sensitivity and poor signal-to-noise ratio (SNR) in dense glandular tissue that is more preponderant in younger premenopausal women (below the age of 40). Furthermore the risks of exposure to radiation limit its applicability, especially for young women with a genetic disposition to develop breast cancer.

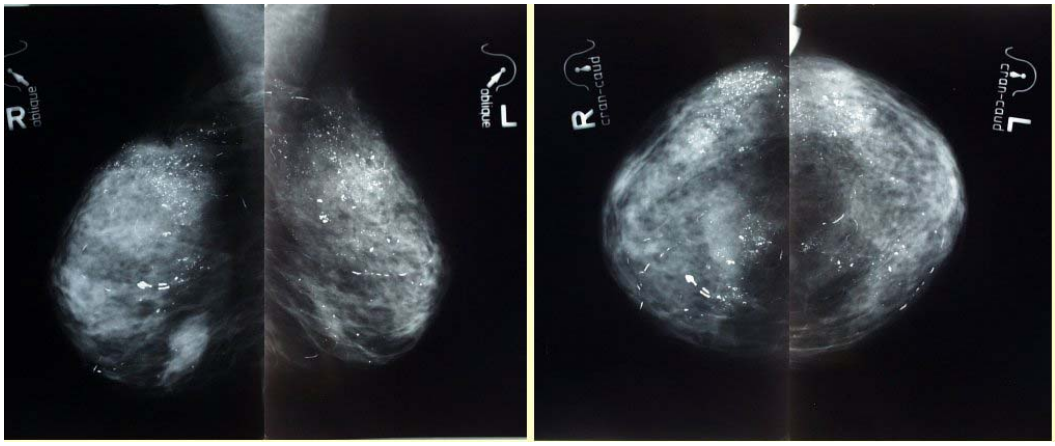

Figure 2.1: Typical x-ray mammogram (left and right) from 2 views.

[3] Sensitivity = true positives/(true positives + false negatives)
Specificity = true negatives/(true negatives + false positives)

[4] The main reason there is high specificity is because most women screened are normal. In actual head to head testing for specific lesions, mammography's specificity is bad, perhaps only slightly better than 50%.

Ultrasonagraphy uses high-frequency sound waves to locate and characterize masses. It is usually used for younger women alongside diagnostic mammography, in answering specific questions about an area of the breast. It is also heavily used to evaluate lesions found on mammography because of its ability to distinguish solid from cystic lesions easily, as well as its ability to guide needle biopsy. As it uses sound waves rather than x-rays, ultrasound provides different and sometimes complementary information to the mammogram. This is especially so in dense breasts where mammography is often unable to visualize tiny tumors without micro-calcifications. In these cases ultrasound may lead to earlier detection of otherwise occult breast cancer. Particularly when breast conservation is contemplated, ultrasound is the modality of choice in the detection of multi-focal tumor foci within the contiguous area of the index lesion.

2.2 CE-MRI mammography

Magnetic resonance imaging (MRI) detects the magnetic resonance induced by low-frequency radiation on hydrogen atoms. MRI has high spatial resolution in tissue because of the specific composition of hydrogen in different tissue types. By applying a magnetic gradient across an object, slices of 3-D tomographic data can be acquired. Hence it does not contain the spatial ambiguity that plagues projective X-ray mammography. With no spatial ambiguity, the location and shapes of lesions can be determined more precisely. A typical MRI slice and the projected volume are shown in Figure 2.2.

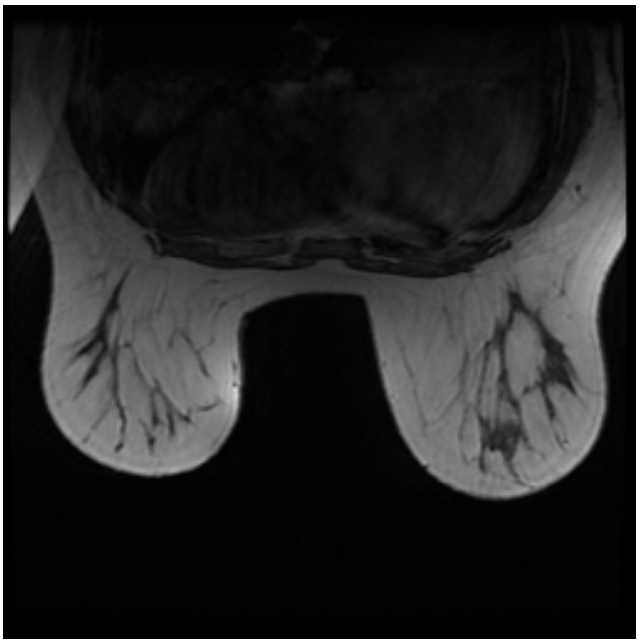

(a)

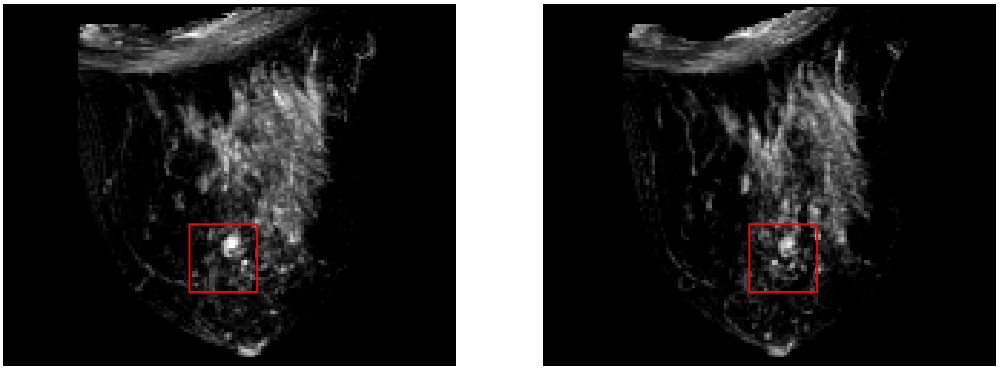

(b) (c)

Figure 2.2: MR mammography – (a) A breast MRI slice; (b) 3D subtracted image maximum intensity projection (MIP); (c) Another MIP taken from another view. High intensity difference regions indicate lesions (boxed), and motion artefacts (present throughout).

However, MRI has low spatial resolution (~1mm in-plane, greater than 3-5mm through-plane). It cannot identify micro-calcifications because of their small size (0.2-0.5mm) and because the modality is inherently insensitive to calcium[5]. Also, MRI requires a longer time (30-60 seconds) for image acquisition, resulting in inevitable patient movement. This in turn results in blurring artefacts (motion within scans) and

[5] Nevertheless CE-MRI may depict the extent of the proliferative intraductal progress in areas of micro-calcifications as well as mammographically occult foci of high-malignant grade DCIS even when micro-calcifications are missing.

motion artefacts (motion between scans). MRI mammography (MRM) also costs eight to ten times more than X-ray mammography[6]. High data storage and transfer bandwidth requirements, as well as a need for novel ways to visualize dynamic 3-D information are also some practical limitations to using MRI in a clinical setting. For a more detailed discussion on MRM please refer to Wang (1999).

Table 2.1: Summary of comparison between X-ray and CE-MRI mammography.

	X-Ray	**CE-MRI**
Dimension	2-D projective, taken from 2 views	3-D tomography, taken in serial scans (5-20 scans), 1 pre-contrast, others post-contrast
Radiation	X-ray (cancer-causing)	Radio-waves (no cancer risk)
Resolution	50μm in 2-D projections	~1mm (in-plane) 3-5mm (through-plane)
Sensitivity	Sensitive in fat	Sensitive in dense glandular tissue
Acquisition time	Instant	30-60 seconds; leads to blurring and motion artefacts

The best way of using MRI in mammography is in contrast-enhanced MRI (CE-MRI), also known as Gd-DTPA MRI (Heywang-Köbrunner & Beck, 1996) or MR mammography (MRM). It requires the intravenous injection of a contrast agent (Gadolinium-pentetate, Gd-DTPA) to give intensity contrast in regions with high vascularity. The increase in signal due to the paramagnetic contrast agent varies approximately linearly with the contrast agent concentration (Buckley *et al.*, 1994), and reveals regions with blood flow and leakage of vessels into the extracellular space of the breast tissue. Malignant cancers are characterized by their angioneogenesis,

[6] Average unsubsidized costs of x-ray mammograms are S$100; MRI costs S$800 excluding contrast-agent. Source: Diagnostic Imaging Department, NUH.

which can be observed by this increase in intensity. The protocol discussed in this paper uses 3-D fast spoiled gradient echo with no spectral fat suppression (TR = 25.6ms, TE=3ms (fractional echo), flip angle = 30^{o}, FOV = 32 to 40cm), performed on a GE Medical Systems Signa 1.5 Tesla clinical whole body MRI unit.

Typically, Gd-DTPA is injected after the first scan, which is followed by four or more post-contrast scans. The enhancement curves are analyzed and matched against expected enhancement curves (Figure 2.3). Essentially, non-lesion tissue and non-tissue regions have little or weak early post-injection enhancement, while lesions usually have high initial enhancements (wash-in). Malignant lesions (carcinoma) will have an earlier incidence of decrease in signal enhancement (wash-out) than benign lesions (fibroadenoma).

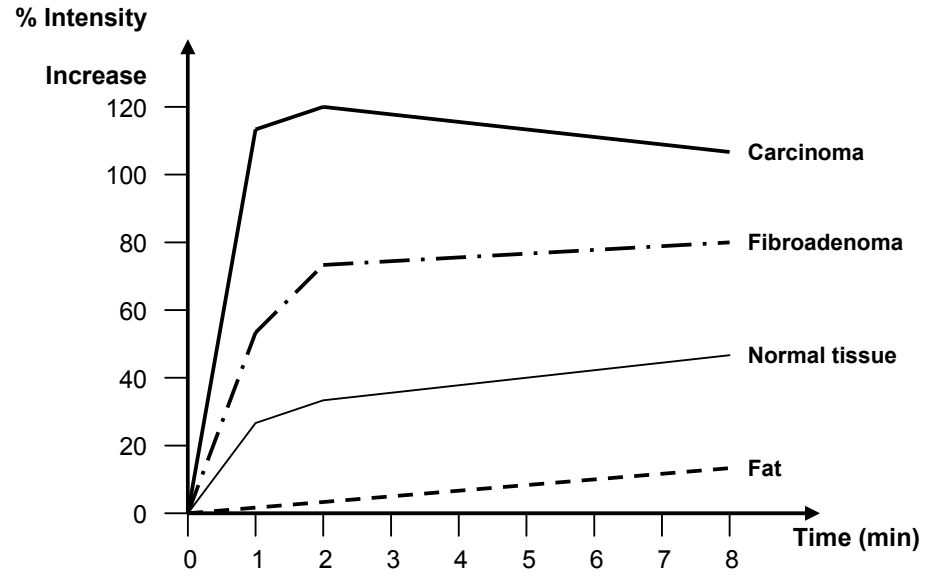

Figure 2.3: Typical signal enhancement curve after injection of Gd-DTP. Adapted from Hayton *et al.* (1997).

Analysis of enhancement curves can be very complicated as CE-MRI is essentially a four-dimensional signal. To simplify this analysis, Degani *et al.* (1997) proposed a

tumor characterization model, 3TP, based on three selected time points on the enhancement curve. The 3TP method uses one pre-contrast (t_0), and two post-contrast (t_1, t_2) values to determine wash-in and wash-out. 3TP was assessed at high spatial resolution on human breast tumors implanted in mice, and later in a clinical trial that had an accuracy of 88% for a variety of breast lesions (Kelcz *et al.*, 2000). For solid lesions of the breast that are larger than 5 mm, sensitivity was 100%.

In another study, the 3TP method was used to determine the importance of spatial resolution in CE-MRI (Furman-Haran *et al.*, 2001). Sensitivity was reduced from 76% to 60% and 24% for a 2- and 4-fold reduction in spatial resolution respectively, while specificity remained largely unaffected. This showed the importance of high spatial resolution to minimize false-negative diagnoses. The corollary was that sensitivity could potentially be increased with greater spatial resolution. This implies that future advancements in resolution can make MRI much more reliable in breast cancer detection.

Enhancement curves do not take into account spatial factors that are also important in determining malignancy. Baum *et al.* (2002) used five classification criteria, including morphological criteria (shape, border), and enhancement criteria (contrast material distribution, initial enhancement, postinitial enhancement) to quantitatively determine malignancy in CE-MRI of the breast via a scoring system (see Table 2.2). Sensitivity and specificity were 92% as found from 522 patients.

One of the key limitations in breast MRI is the very large number of images produced by such sequential enhancement imaging. This currently involves labour intensive and

expert human reader analysis, which is one of the main reasons the test is so expensive. Introducing a quantitative scoring method that includes spatial criteria in diagnosing breast cancer using CE-MRI could potentially lead to an automated system for mass-screening with CE-MRI. This would not only greatly reduce the time required for interpretation but potentially increase the accuracy over many human readers, thus reducing the cost of the procedure.

Table 2.2: Scoring system proposed by Baum *et al.* (2002)

Points	**0**	**1**	**2**
Shape	Round	Dendritic	-
	Oval	Irregular	
Border	Well-defined	Ill-defined	-
Contrast material distribution	Homogeneous	Inhomogeneous	Rim
Initial enhancement[a]	<50%	50-100%	>100%
Postinitial enhancement[b]	Continous increase[c]	Plateau[d]	Wash out[e]

[a] $Signal_{initial}=(Signal_{max1\text{-}3min} - S_{precontrast})$: $S_{precontrast}$ x 100 (%);
[b] $(Signal_{8\ min} - Signal_{max1\text{-}3min})$: $S_{max1\text{-}3min}$ x 100 (%);
[c] More than 10%; [d] +10% to –10%; [e] Less than –10%

Despite the relatively high levels of sensitivity and specificity found in these studies (Degani *et al.*, 1997; Furman-Haran *et al.*, 2001; Baum *et al.*, 2002), CE-MRI at best is only used for secondary diagnosis. Currently, the dominant indications (uses) of MRI mammography are in women with dense breasts, silicone implants, and in cases where suspected lesions found in X-ray mammograms require another imaging modality to characterize abnormalities (see Wang (1999) for a detailed list of MRI indicators). While future improvements in imaging speed and resolution and lower costs can address the shortfalls of MRI (including blurring artefacts), motion artefacts resulting from the dynamic aspect of CE-MRI will remain. This motion, which can be due to inadvertent breathing or arbitrary movements due to discomfiture (especially after

injection of the contrast-agent), is in a non-rigid manner as the breast is a flexible object not bounded by bones. Despite innovations in visualization of dynamic CE-MRI mammography (Choi *et al.*, 2002), motion (especially those involving movements between acquired slices) needed to be accounted for. Figure 2.4 shows an example of motion artefacts arising from digital subtraction between post- and pre-contrast slices. While most artefacts on the boundary of the breast may be segmented visually, the problems of internal motion artefacts remain. Practically, it is tedious to manually segment artefacts or align scans because of the large 3-D dynamic dataset for each patient.

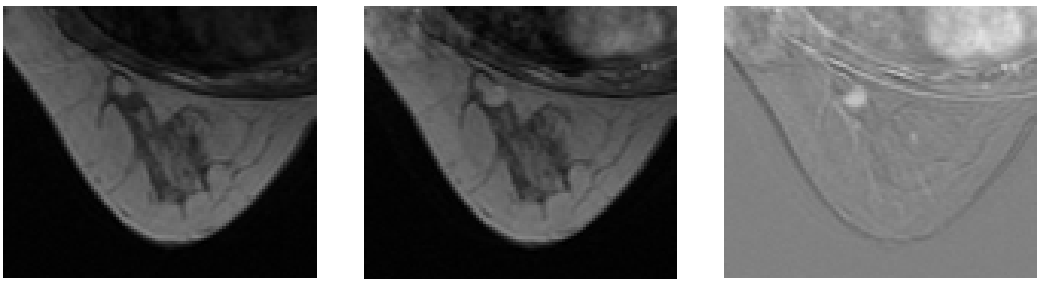

(a) (b) (c)

Figure 2.4: Misalignment of images shown after subtraction. (a) Pre-contrast image, (b) post-contrast image, and (c) subtracted image. Motion artefacts are present around the boundary of and inside the breast, in addition to the presence of an obvious lesion.

2.3 Medical image registration

Aligning a dynamic sequence of CE-MRI mammography images requires a process to model the motion between the sequences. This process is known as image registration. Image registration establishes physical correspondences between sets of images by modeling processes that include not only motion, but also non-uniform intensity changes due to time, difference in image acquisition techniques and other environment variables. In image registration, finding the parameters is just a means to an end; the

emphasis in image registration is the integration of information. This implies that the transformation must be accurate to the finest resolution required within the region(s) of interest. A task that uses the same processes as image registration is image fusion, which emphasizes the visualization of combined images from multiple modalities.

Advances in image registration are predominantly in applications in medical images. Medical image registration is the fusion of medical images from the numerous imaging modalities such as computed tomography (CT), x-rays, MRI, ultrasound, positron-emission tomography (PET), etc. Fusion of information is not limited to image information only. Information from spatially sparse inputs such as EEG (electro-encephalography) and MEG (magnetic-encephalography) gives rise to the term functional imaging, which in this literature is considered a separate but related task.

A very thorough survey on medical image registration was done by Maintz and Viergever (1998). They provided a standard classification for registration procedures that had nine criteria that were further divided into primary sub-divisions. The criteria may also be broadly organized into three parts – problem statement, registration paradigm and optimization procedure. Registration of CE-MRI mammography stands out in medical image registration literature because it is one of few applications that model motion from a single imaging modality. This classification is summarized in Table 2.3.

Table 2.3: Criteria of Medical Image Registration.

Criteria	Sub-division	Parts
Dimensionality	-	Problem statement
Nature of registration basis	Extrinsic, intrinsic, non-image based	Registration paradigm
Nature of transformation	Rigid, affine, projective, curved	Problem statement & registration paradigm
Domain of transformation	-	Problem statement & registration paradigm
Interaction	-	Registration paradigm, optimization procedure
Optimization procedure	-	Optimization procedure
Modalities involved	Monomodal, multi-modal, modality to model, patient to modality.	Problem statement
Subject	Intersubject, intrasubject, atlas.	Problem statement
Object	-	Problem statement

2.4 Registration techniques in mammography

The problem of registration of dynamic MRM is defined as the intrasubject (subject) registration of the breast (object) in a single modality (modalities involved) that is three-dimensional (dimensionality), and that corrects misalignment of the breast between dynamic contrast-enhanced scans caused by patient movement. As the breast is a flexible object, the registration must model local deformation (domain of transformation) using some curved transformation (nature of transformation). This problem neither favors the use of extrinsic markers nor interactivity because of the high-order of deformation required. Thus registration has to be intrinsic (registration basis) and mostly automatic (interaction).

Registration of dynamic breast MRM uses one volume as the positional frame of reference. The pre-contrast volume is usually used as the reference, and subsequent post-contrast volumes are registered to it. Zuo *et al.* (1996) proposed using the Woods

algorithm (1992) that minimizes the ratio of variance between images. This algorithm however assumes that the breast is characterized by rigid motion only, which cannot be used for local motion modeling. Kumar *et al.* (1996) and Fischer *et al.* (1999) proposed using an optical-flow technique for non-rigid registration. However, it assumes that the intensities between the images compared for registered must be constant. It therefore does not account for the increase in intensity due to the contrast agent.

In order to model non-uniform intensity change, Hayton *et al.* (1997) used a pharmacokinetic model with the optical flow-algorithm to register 2-D MRI mammograms. It relies on the assumption that the change of intensities follows the pharmacokinetic model, which is not always the case due to factors like non-isotropic sampling, magnetic gradient bias effects, motion-blurring, and aliasing (due to motion and sampling) that occur typically. This led to a non-rigid registration algorithm using Bayesian estimates of motion fields derived from optical flow, using mutual information (MI) as the cost function (Hayton *et al.*, 1999).

Combining global and local motion modeling, Rueckert *et al.* (1999) proposed optimizing normalized mutual information (NMI) to account for both non-rigid motion and non-uniform changes in intensity. NMI, as proposed for use in image registration by Viola (1995) and Studholme (1999), is a better registration cost function because it is independent of image overlap. One disadvantage of entropy measures like MI and NMI are its immense computational costs, especially for non-rigid optimization.

To speed up computation in a clinical setting, Rainer and Aldo (2001) proposed a parallel implementation using self-organizing maps (SOM) without using any

transformation model. Reichenbach *et al.* (2002) suggested a compromise between rigid and non-rigid registration, by using slice-wise rigid registration with subsequent interpolation between slices with MI. This approach however could only model slice-by-slice rigid transformations, and discounted tissue deformations caused by the compressibility of the breast.

To verify the accuracy of registration, quantitative and qualitative measurements might be used. Intensity-based measurements include sum-of-squared differences (SSD) (Rueckert *et al.*, 1999; Tan *et al.*, 2003B), absolute differences (Hayton *et al.*, 1997), and correlation coefficient (Rueckert *et al.*, 1999; Fischer *et al.*, 1999); distance-based measurements include mean-square registration errors (Hayton *et al.*, 1997); and information based measurements are derived from MI (Reichenbach *et al.*, 2002; Tan *et al.*, 2003A). All authors reported significant visual improvements after registration. Rueckert *et al.* provided a qualitative ranking system using the assessments from two radiologists to compare different transformations. They showed that rigid and affine registrations were comparable, while non-rigid registrations were mostly better than rigid registration alone. Inverse transfer functions were also compared to check for consistency of solutions (Hayton *et al.*, 1999). Reichenbach *et al.* (2002) also used a phantom to verify registration accuracy, but the phantom was only manipulated rigidly.

Different types of patient movements were also evaluated in controlled experiments. These included variations in speeds and amplitudes of breathing (Rueckert *et al.*, 1999; Fischer *et al.*, 1999), voluntary patient movement (Rueckert *et al.*, 1999; Fischer *et al.*, 1999), coughing (Rueckert *et al.*, 1999), and tensing and relaxation of pectoral muscles which affect movement of the Coopers ligaments (Hayton *et al.*, 1999). The general

consensus were that motion resulted in blurring that worsened quantitative and visual assessments, and that registration continued to provide better assessments albeit worse than cases without prescribed motion. To computationally verify the accuracy of non-rigid registration, Schnabel *et al.* used finite element modeling (FEM) to assess the Rueckert's algorithm using a biomechanical model (Schnabel *et al.*, 2003). They found that a higher degree of registration error was present in regions with tumors for pre-contrast to post-contrast registration, and that the tumor volume was not preserved.

While registration models the motion of the breast, the motivation behind CE-MRI is mainly in cancer detection. Most registration attempts compare two volumes without considering information from known contrast-enhancement profiles. By incorporating pattern recognition only after non-rigid registration, Fischer *et al.* (1999) used self-organizing maps (SOM) to classify tissue as benign or malignant. While SOM offered an automatic way of grouping tissue, the grouping was dependent on the training data which are not necessarily representative of all contrast-enhancement profiles.

Other tasks related to CE-MRI registration include biomechanical modeling of the breast (Tanner *et al.*, 2001; Azar *et al.* 2002), and registration between MRI and X-ray mammograms (Behrenbruch *et al.*, 2003; van Engeland *et al.*, 2003). The motivations behind these were in predicting mechanical deformations during needle breast procedures (Azar *et al.*, 2002), and in modeling the compression of breast during X-ray mammography (Tanner *et al.*, 2001; Behrenbruch *et al.*, 2003; van Engeland *et al.*, 2003).

2.5 Proposed approach

Our motivation is to create a registration system to remove or reduce motion artefacts present in CE-MRI scans to render registered images usable in clinical settings. Accurately registered scans should display the correct enhancement curves. This is the requirement for any clinical application and is also the premise for using a contrast agent. This project strives for pixel-resolution accuracy, robustness and the efficiency required for clinical implementation. Rueckert's algorithm has been verified using biomechanical models. However, NMI computation is very expensive; the algorithm does not use any information relating the contrast enhancement curve and inaccuracies can occur as shown by the reduction of lesion volumes.

Previously, a new NMI-based adaptive cost function was proposed to improve accuracy and speed (Tan *et al.*, 2003A), and the effects on enhancement curves due to registration were examined (Tan *et al.*, 2003B). The challenges that remain are (i) whether a more intuitive cost function can improve the accuracy and speed of registration, and (ii) whether registration will result in improved detection rates.

In answering the first challenge, a contrast enhancement model was proposed to simplify NMI calculations, using an adaptation from estimating Gaussians in entropy calculation (Leventon & Crimson, 1998). This model was combined with the thoroughly tested 3TP method in registration. To meet the second challenge, the 3TP method was also used to compare registration results so as to make the comparisons more meaningful in a clinical sense, in addition to using measurements of registration quality and visual comparisons from a clinical reader.

CHAPTER THREE

THEORY

3.1 Geometric transformations

Motion models may be described using geometric transformations that are commonly used in various mathematics and science disciplines. The parameters that characterize the transformations determine the number of degrees of freedom. The registration task involves modeling motion. The appropriate transformations used to model the motion should be chosen according to the efficiency, effectiveness, and robustness of its parameters. The motion models used can be divided into global and local models.

3.1.1 Global motion model

A global motion model is applied to the entire signal, as opposed to a local motion model. There are several classes of geometric transformations that are used in global motion models. Rigid transformations in IR^3 have 6 degrees of freedom, involving translations along and rotations about the three cardinal axes; they preserve all lengths and angles between lines. Affine transformations include rigid transformations, as well as scaling (dilation) and shearing; they preserve the proportion of lengths of parallel lines, but do not preserve their lengths and angles. Denoting R as the rotation matrix, θ_x, θ_y, θ_z as the angles of rotation and $[t_x, t_y, t_z]$ as the translation vector, the general form of an affine transformation is:

$$T_R(x,y,z) = R\begin{bmatrix} x \\ y \\ z \end{bmatrix} + \begin{bmatrix} t_x \\ t_y \\ t_z \end{bmatrix}$$

$$= \begin{bmatrix} R_{11} & R_{12} & R_{13} & t_x \\ R_{21} & R_{22} & R_{23} & t_y \\ R_{31} & R_{32} & R_{33} & t_z \\ 0 & 0 & 0 & 1 \end{bmatrix} \begin{bmatrix} x \\ y \\ z \\ 1 \end{bmatrix} \quad \ldots(1)$$

The rotation matrix, *R* is defined as:

$$R = \begin{bmatrix} R_{11} & R_{12} & R_{13} \\ R_{21} & R_{22} & R_{23} \\ R_{31} & R_{32} & R_{33} \end{bmatrix} = \begin{bmatrix} \cos\theta_z & -\sin\theta_z & 0 \\ \sin\theta_z & \cos\theta_z & 0 \\ 0 & 0 & 1 \end{bmatrix} \begin{bmatrix} \cos\theta_y & 0 & \sin\theta_y \\ 0 & 1 & 0 \\ -\sin\theta_y & 0 & \cos\theta_y \end{bmatrix} \begin{bmatrix} 1 & 0 & 0 \\ 0 & \cos\theta_x & -\sin\theta_x \\ 0 & \sin\theta_x & \cos\theta_x \end{bmatrix}$$

Global motion models applied in registration tasks are also known as rigid registration. Affine transformations are commonly used in multi-modality image registration (Wells *et al.*, 1996; Leventon & Crimson, 1998; Studholme *et al.*, 1999; Loew & Carranza, 1998; Maes *et al.*, 1999) when the intensity mappings of the image are non-uniform. To reduce the dimensionality of the search space, images may be scaled or sub-sampled to obtain images of the same scale prior to optimization of other affine parameters.

3.1.2 Local motion model

Local or adaptive motion models employ transformations with a much higher degree of freedom. The optimization of local motion parameters is known as non-rigid registration.

In addition to being used in interpolation and curve-matching, spline models are commonly used in creating local motion models. The power and complexity of a spline model increases with the order of the spline. In image registration, 3rd order B-Splines are used to balance power and efficiency, and may be employed hierarchically for multi-resolution registration (Szeliski & Coughlan, 1994; Kumar *et al.*, 1996; Fischer *et al.*, 1999; Rueckert *et al.*, 1999; Hayton *et al.*, 1999). A simplified form is in the use of thin-plate splines (Likar & Pernuš , 2001). Figure 3.1 shows how a B-Spline mesh can be manipulated in 2-D.

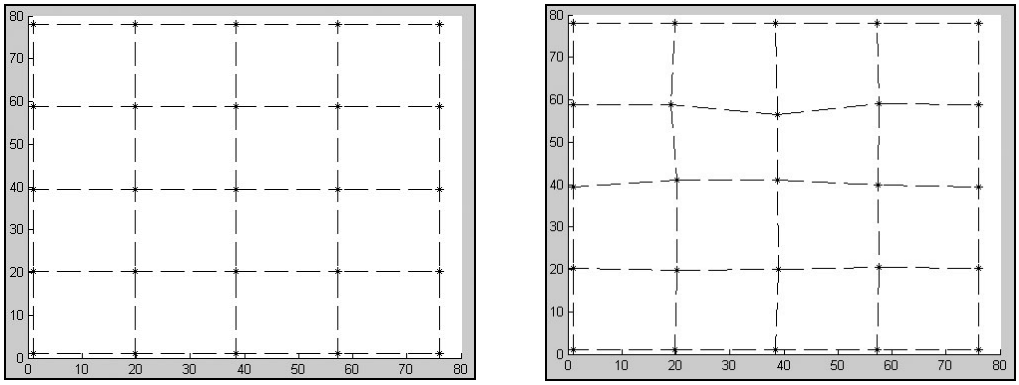

(a) (b)

Figure 3.1: Mesh of control points on a 2-D Plane (a) prior to manipulation and (b) after manipulation using B-Splines.

Denoting the domain of the image volume as $\Omega = \{(x, y, z) \mid 0 \le x < X, 0 \le y < Y, 0 \le z < Z\}$, let Φ represent a 3-D set of control point co-ordinates $\phi_{i,j,k}$, with a size of (n_x, n_y, n_z) and a uniform spacing of $(\delta_x, \delta_y, \delta_z)$ .The indexes are defined as $i = \lfloor x/\delta_x \rfloor - 1$, $j = \lfloor y/\delta_y \rfloor - 1$, $k = \lfloor z/\delta_z \rfloor - 1$, and $u = x/\delta_x - \lfloor x/\delta_x \rfloor$, $v = y/\delta_y - \lfloor y/\delta_y \rfloor$, $w = z/\delta_z - \lfloor z/\delta_z \rfloor$. In $\mathbb{R}^3$, B-Splines may be expressed as a trifocal tensor of its coefficients and coordinates:

$$T_{NR} = \sum_{l=0}^{3}\sum_{m=0}^{3}\sum_{n=0}^{3} B_l(u)B_m(v)B_n(w)\phi_{i+l,j+m,k+n} \quad \ldots(2)$$

$B_l(u)$ represents the l^{th} basis function of the B-Spline for an interval u:

$$B_0(u) = (1-u)^3/6,$$
$$B_1(u) = (3u^3 - 6u^2 + 4)/6,$$
$$B_2(u) = (-3u^3 + 3u^2 + 3u + 1)/6,$$
$$B_3(u) = u^3/6$$

In multi-resolution non-rigid registration using B-Splines, the net transformation may be expressed as a summation of rigid and non-rigid transformations:

$$T = T_R + \sum_{\delta} T_{NR,\delta} \quad \ldots(3)$$

The deformation field in image registration may also be modeled as a linear combination of a set of radial basis functions (RBFs). Where r is the Euclidean or absolute radius, and the basis function is Gaussian, RBFs may be defined as:

$$\Phi(r) = \exp\left(-\frac{r^2}{2\sigma^2}\right) \quad \ldots(4)$$

Other common basis functions include quadric variants (multi-quadric, inverse multi-quadric), thin plate spline ($\Phi(r) = r^2 \ln r$), cubic, and linear functions. The advantage of using RBFs is that it can be computationally efficient while physically feasible, provided that the centers and other parameters are initialized well. Methods of choosing centers include random selections, orthogonal least-squares, and k-means clustering. RBFs are commonly applied in atlas registration (Fornefett *et al.*, 2001;

Rohde *et al.*, 2003), which registers new images to an image (atlas) representative of the population.

3.2 Volume registration

The nature of registration basis considered here is intrinsic registration or volume registration, which uses pixel/voxel attributes such as intensity to determine motion parameters. As opposed to surface registration techniques which are based on point correspondences, volume registration requires establishing a relationship between intensity voxel attributes and motion.

3.2.1 Optical flow

Optical flow, as proposed by Horn and Schunck (1981), is the relationship between brightness variation in an image and the motion field. It has been used in many computer vision tasks such as camera calibration and motion estimation. Registration can be used to estimate motion. The fundamental equation of motion analysis is the image brightness constancy equation.

Lemma: The *image brightness constancy equation* assumes that the image brightness, E, is a function of both spatial and temporal coordinates; that E is continuous and differentiable as many times as needed in both the spatial and temporal domain; and that the apparent brightness of the moving object is constant. Then, the summation of partial derivatives of E with respect to spatial and temporal variables should be zero:

$$(\nabla E)^T v + E_T = 0 \qquad \ldots(5)$$

In $\mathbb{R}^3$, the Jacobian operator, $\nabla(\cdot) = \left(\frac{\partial}{\partial x}, \frac{\partial}{\partial y}, \frac{\partial}{\partial z}\right)(\cdot)$

In $\mathbb{R}^3$, the motion field, $v = \left(\frac{dx}{dt}, \frac{dy}{dt}, \frac{dz}{dt} \right)$

Temporal partial derivative, $E_T = \frac{\partial E}{\partial t}$.

Defining Δ as a small but finite spatial interval, the discrete spatial derivative (finite spatial gradient) is:

$$\frac{\partial E(x, y, z, t)}{\partial x} \cong \frac{E(x + \Delta) - E(x)}{\Delta} \qquad \ldots(6)$$

Variations of the gradient computation depend on the type and size of low-pass filter masks.

The assumption of the ability to obtain spatial derivatives implies that optical flow can only specify motion within the interval of resolution of the spatial derivatives. Thus it will fail to model motion with displacements greater than Δ. In such instances, multi-resolution strategies employing variable spatial intervals and filters should be used.

Another problem associated with optical flow is the aperture problem, whereby the component of the motion field in the direction orthogonal to the spatial image gradient is not constrained by the image brightness constancy equation. In registration, this problem is more acute in local motion field modeling because the parameters only have local reach, as opposed to the global reach in global affine models. Multi-resolution strategies in local field modeling can reduce this problem by providing more accurate coarse alignments at lower resolutions prior to more precise alignments at higher resolutions.

3.2.2 Cost functions

Optical flow assumes that image brightness is constant, which may not be the case in image registration. In multi-modality registration, the image brightness (intensity) mapping between images from different modalities is non-linear and is many-to-many. Thus inverse intensity mappings generally do not necessarily correspond.

Adapting from the contrast brightness equation, another property derived from intensity may be assumed to be constant instead. The cost function, defined in optimization procedures, is derived from that property.

When the constant property is intensity, the cost function is a sum-of-squares difference (SSD) of intensity, defined as:

$$SSD = \sqrt{\frac{\sum_{i}^{n} \left(E_i - E_i'\right)^2}{n}} \quad \forall i \in E \cap E', \qquad \ldots(7)$$

where E is the reference image and E' is the registered image.

A variation of SSD is NSSD (negative sum-of-squares), which is useful in estimating the amount of motion artefacts in CE-MRI, as intensities are expected to increase rather than to decrease after the injection of the contrast agent. NSSD is different from SSD because it only includes pixels that result in negative changes in intensity. This is defined as:

$$NSSD = \sqrt{\frac{\sum_{i}^{n} \left(E_i - E_i'\right)^2}{n}} \quad \forall i \in E \cap E' \cap \left\{\left(E' - E\right) < 0\right\} \qquad \ldots(8)$$

Another cost function commonly used is the correlation coefficient (CC), which is defined as:

$$CC = \frac{\sum_{i}^{N}\left(E_i - \overline{E}\right)\left(E_i' - \overline{E'}\right)}{\sqrt{\left\{\sum_{i}^{N}\left(E_i - \overline{E}\right)^2 \sum_{i}^{N}\left(E_i' - \overline{E'}\right)^2\right\}}} \quad \forall i \in E \cap E' \qquad \ldots(9)$$

SSD and NSSD are at their minimum when the images are optimally aligned, while CC is at its maximum when the images are optimally aligned. Computationally, SSD and NSSD are $O(n)$ operations while CC is $O(3n)$.

Mutual information (MI) is used instead of SSD and CC in multi-modality registrations because it can account for non-uniform changes in intensity. Denoting $p(s)$ is the probability of occurrence of the intensity, *s* in the intensity range, the entropy commonly used is Shannon's entropy, defined as:

$$H = -\sum_{s} p(s)\log(p(s)) \qquad \ldots(10)$$

MI is defined as:

$$MI(E, E') = H(E) + H(E') - H(E, E') \qquad \ldots(11)$$

In registering one image to another there are two random variables. The entropies used here are the marginal entropies $H(E), H(E')$ as well as joint entropy $H(E, E')$. These are based on the definitions of marginal probability and joint probability respectively.

Normalized MI (NMI) has also been proposed in place of MI. It has been shown to be overlap invariant (Studholme *et al.*, 1999), and have been used as a cost function in multi-modality registration too. Denoting NMI as $\mathrm{Y}(E, E')$ when found as a function of two inputs:

$$\mathrm{Y}(E, E') = \frac{H(E) + H(E')}{H(E, E')} \quad \ldots(12)$$

When images are optimally aligned, the resulting intensity mappings will correspond, resulting in lower joint entropy. Thus MI and NMI will be at maximum when the images are aligned (see Figure 3.2). Computationally, MI and NMI are at least $O(n^2)$ operations.

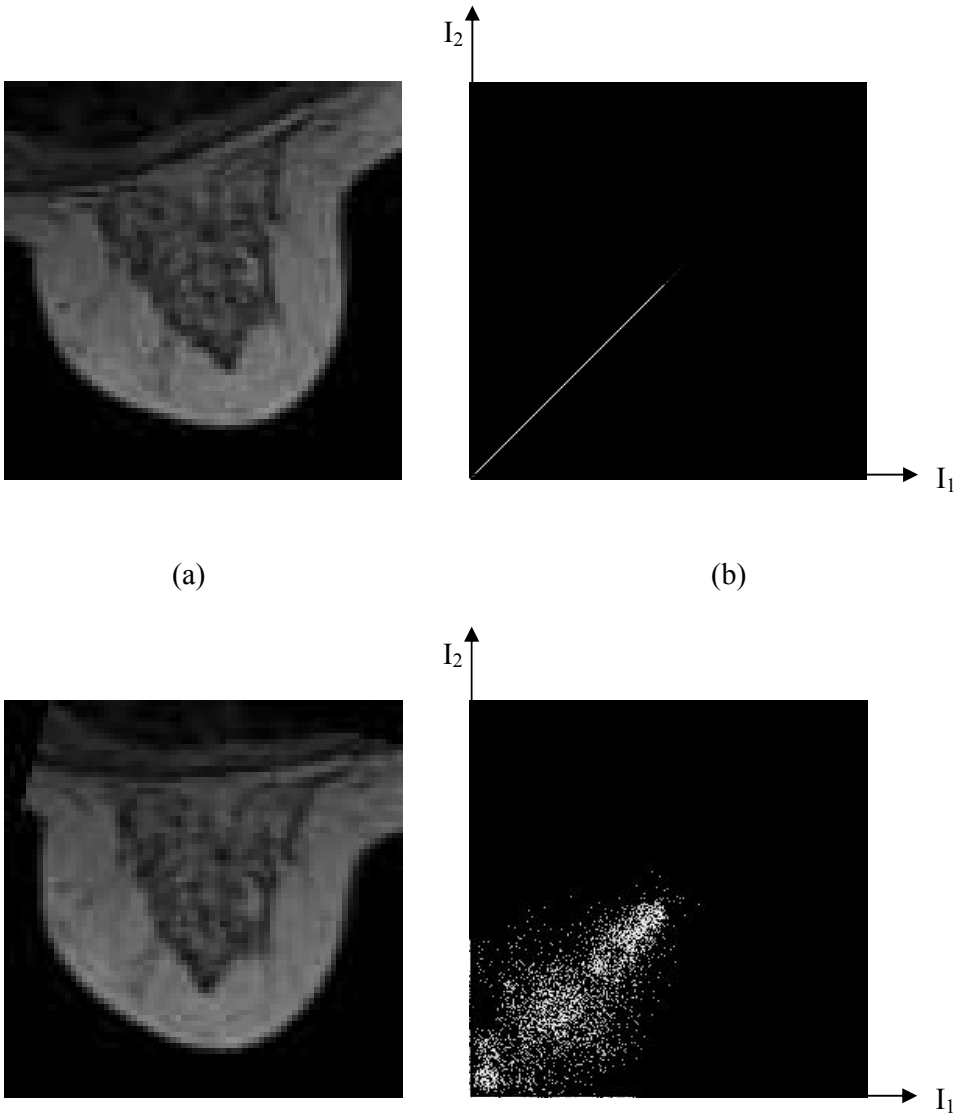

Figure 3.2: 2-D Images of breast MR slices. (a) Original image; (b) JPDF of original image against itself; (c) Image rotated clockwise by 15 degrees; (d) JPDF between (a) and (d).

3.3 Computing NMI

Finding MI or NMI is more computationally expensive, when compared to finding SSD or CC, because the histograms of both images need to be found. Generally, image intensities are not integer values, so it will be required to estimate the contributions to the probability densities. Estimation methods add to the computational complexity.

There are two main approaches to estimation. The first involves interpolation, which includes nearest neighbor (NN) interpolation, and linear interpolation; the second involves computing the contributions of each sample to each intensity bin analytically. The first method is straightforward, but does not allow analytical computation of the contributions; the second allows analytic computation of the histogram derivative, allows a wider range (not just the two nearest integer intensities), but requires normalization of the contributions. In general, the first approach is termed interpolation and the second is termed density estimation, but the difference really is in the kernel size.

An alternative to the second approach is that if the probability density functions (PDFs) of the images can be parameterized, simplifications can be made to reduce the computational complexity.

3.3.1 Linear interpolation and partial volume interpolation

Interpolation methods of finding the histogram generally did not allow analytic computation of the derivative of the histogram, because the weights of the contributions from each sample are not stored while the histogram is computed. As such, gradient estimation methods such as Powell's level set method had to be used to

compute the image gradient with respect to entropy measures. To circumvent this problem, Collignon (1995) and Maes (1997) introduced partial volume (PV) interpolation, which was the same as linear interpolation except that the contribution weights to each sample are stored to allow analytic computation of the derivative of the histogram with respect to each sample. The histogram probability function is:

$$P(x,\alpha) = \frac{1}{N_\alpha} \sum_{x_\alpha \in \alpha} w_{x-x_\alpha} \delta(x - x_\alpha) \qquad \ldots(13)$$

Denoting α as the set of samples, x_α is a sampled intensity, N_α is the total number of samples in the image, δ is a discrete unit pulse, and w is the weight contribution. By considering the subset of points in the entire image that fall within one unit of intensity of difference from the intensity bin x, the summation via PV interpolation is the equivalent to linear interpolation except that if the derivative of the weights can be found, then the derivative of the probability can be expressed analytically. The derivation of this derivative is shown in the next section.

A comparison between linear and PV interpolation by Pluim *et al.* (2000) revealed the presence of interpolation artefact patterns in both types of interpolations. This indicates that interpolating between the nearest two intensities does not provide good generalization in registration. A larger kernel size is needed in finding the weight contributions to the histogram.

3.3.2 Parzen density estimation

Parzen density estimation, as independently proposed by Collignon (1995) and Viola (Viola, 1995), allows the use of larger kernels. The fundamental difference is that each sample has a density function instead of having weighted sums of discrete unit pulses

as found using interpolation. In image registration it has been used to compute PDFs (Wells *et al.*, 1996). It is a non-parametric method, where the samples are used to define the parameters of the PDF. This is applicable to stochastic processes like images.

The general form of the estimated probability function is:

$$P(x,\alpha)=\frac{1}{N_\alpha}\sum_{x_\alpha\in\alpha}R(x-x_\alpha) \qquad \ldots(14)$$

where α is a sample, N_α is the total number of samples in the image, and R is a valid density function, also known as the smoothing or window function. The common density function used is the Gaussian function, making the Parzen estimate a summation of Gaussian functions centered on each intensity sample. Previously in PV-interpolation, R would have taken the form of a linear function across two window levels (intensity bins). The derivative of the weights would have been found using a discrete method that is not smooth. Figure 3.3 illustrates how probability may be estimated based on the distribution of a Gaussian function of variance ψ centered on an intensity mean, $\bar{x}$. Probability contributions to the nearby integer intensity bins, $p^*(x)$, may be found using the 1-D or 2-D Gaussian PDF:

$$\text{1-D: } p^*(x)=\frac{1}{\sqrt{2\pi\psi}}\exp\left(-\frac{(x-\bar{x})^2}{2\psi}\right) \qquad \ldots(15)$$

$$\text{2-D: } p^*(x,y)=\frac{1}{2\pi\psi}\exp\left(-\frac{(x-\bar{x})^2+(y-\bar{y})^2}{2\psi}\right) \qquad \ldots(16)$$

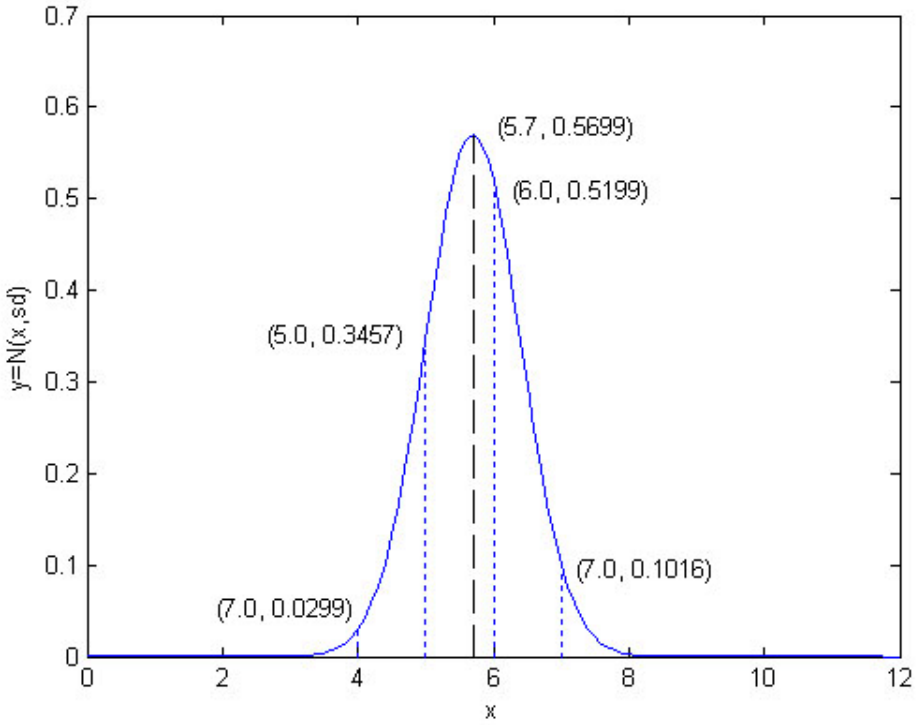

Figure 3.3: 1-D Gaussian distribution centered on non-integer mean (x=5.7), used to interpolate the contributions to the histogram at integer positions.

Other suitable density functions may be used, but the Gaussian distribution is also a convenient one. When differentiated with respect to its mean, the result is a factor of itself:

$$\frac{\partial g_{\psi}\left(x-\bar{x}\right)}{\partial \bar{x}} = g_{\psi}\left(x-\bar{x}\right)\psi^{-1}\left(x-\bar{x}\right) \qquad \ldots(17)$$

The derivatives of marginal and joint PDFs with respect to a transformation variable ϕ are thus:

$$\frac{\partial P(X=x)}{\partial \phi} \cong \sum_{i}^{i_{\max}} g_{\psi}\left(x-\overline{x_i}\right)\psi^{-1}\left(x-\overline{x_i}\right)\frac{\partial \overline{x_i}}{\partial \phi}$$
$$\frac{\partial P(Y=y)}{\partial \phi} \cong \sum_{j}^{j_{\max}} g_{\psi}\left(y-\overline{y_j}\right)\psi^{-1}\left(y-\overline{y_j}\right)\frac{\partial \overline{y_j}}{\partial \phi} \qquad \ldots(18)$$
$$\frac{\partial P(X=x,Y=y)}{\partial \phi} \cong \sum_{i,j}^{i_{\max},j_{\max}} g_{\psi}\left(x-\overline{x_i},y-\overline{y_j}\right)\psi^{-1}\left(y-\overline{y_j}\right)\frac{\partial \overline{y_j}}{\partial \phi}$$

The derivative of NMI with respect to ϕ using Parzen density estimation is:

$$\frac{\partial \mathrm{Y}}{\partial \phi} = H(E,E')\left(\frac{\partial H(E')}{\partial \phi} - \mathrm{Y}\frac{\partial H(E,E')}{\partial \phi}\right)$$
$$= -\frac{1}{H(E,E')}\left(\sum_{y}(1+\log P(y))\frac{\partial P(y)}{\partial \phi} - \mathrm{Y}\sum_{x,y}(1+\log P(x,y))\frac{\partial P(x,y)}{\partial \phi}\right) \qquad \ldots(19)$$

The choice of variance and the Parzen window size is crucial to both the sensitivity of the derivative and computational efficiency. Also, a relatively wide window size will be required if normalization were to be neglected. It was found empirically that window sizes of [-3, +3] or [-4, +4], with variances that resulted in extreme sample values that are 1% of the peak value, were reasonably sensitive and efficient.

3.3.3 Multivariate Gaussian Estimation

If the PDFs of the images may be parameterized using standard distributions, computation of entropy may be simplified. Gaussians have been used to estimate the joint PDF (JPDF) (Leventon & Crimson, 1998) using expectation maximization to parameterize the JPDF as Gaussians in multi-modality registration. However, the main difficulty of using expectation maximization is in finding the number of parameters to be estimated. Thus interpolation techniques and Parzen density estimation have been advocated over estimating the JPDF as Gaussians.

CE-MRI registration may be considered a special case of non-uniform intensity registration where estimating PDFs as Gaussians is suitable. Instead of modeling the joint PDF, assume that the conditional PDF can be modeled instead. The conditional PDF with respect to *E'* can be defined as:

$$H(E \mid E') = -\sum_{Y}\sum_{X} P(X = x, Y = y)\log\left(P\left(X = x \mid Y = y\right)\right) \quad \ldots(20)$$

Consider $P(X = x \mid Y = y) \forall\, Y \;\Rightarrow\; N\left(m_y, \sigma_y^2\right)$, i.e., the conditional PDF can be modeled as a 1-D Gaussian distribution for all integer values of *Y*, where each integer value of *Y* has a mean and variance defined by:

$$\begin{aligned} m_y &= \sum_{X} P\left(X = x \mid Y = y\right)x \\ &= E\left(X \mid Y = y\right) \\ \sigma_y^2 &= \sum_{X} P\left(X = x \mid Y = y\right)\left(x - m_y\right)^2 \\ &= E^2\left(X \mid Y = y\right) - E\left(X \mid Y = y\right)^2 \end{aligned} \quad \ldots(21)$$

The conditional entropy with respect to *E'* can be expressed as:

$$\begin{aligned} H(E \mid E') &= -\sum_{Y}\sum_{X} P(X = x, Y = y)\log\left(\frac{1}{\sqrt{2\pi}\sigma_y}\exp\left(-\frac{\left(x - m_y\right)^2}{2\sigma_y^2}\right)\right) \\ &= \frac{1}{2}\log(2\pi) + \sum_{Y} P(Y = y)\log\left(\sigma_y\right) + \sum_{Y}\sum_{X} P(X = x, Y = y)\frac{\left(x - m_y\right)^2}{2\sigma_y^2} \end{aligned} \quad \ldots(22)$$

Let the mapping functions $f_{x1} : x \to \frac{x}{\sqrt{2}\sigma_y}$, $\quad f_{y1} : y \to \frac{m_y}{\sqrt{2}\sigma_y}$ create two new signals *A* and *B* that are defined by:

$$A = E\left(f_{x1}(X = x)\right), \quad B = E'\left(f_{y1}(Y = y)\right) \quad \ldots(23)$$

Then conditional entropy may be expressed as:

$$H(E \mid E') = \frac{1}{2}\log(2\pi) + \sum_{Y} P(Y = y)\log(\sigma_y) + \sum_{Y}\sum_{X} P(X = x, Y = y)(x' - y')^2$$
$$= \frac{1}{2}\log(2\pi) + \sum_{Y} P(Y = y)\log(\sigma_y) + SSD(A, B) \quad \ldots(24)$$

where SSD*(A,B)* is the sum-of-squares function.

Similarly, the conditional PDF with respect to *E* if assumed to be Gaussian for all *X* is:

$$H(E' \mid E) = \frac{1}{2}\log(2\pi) + \sum_{X} P(X = x)\log(\sigma_x) + SSD(A', B') \quad \ldots(25)$$

The definitions for both conditional PDFs are summarized in Table 3.1.

Table 3.1: Summary of definitions used in multivariate Gaussian estimation for conditional PDFs.

	$H(E \mid E')$	$H(E' \mid E)$
Conditional mean	$m_y = E(X \mid Y = y)$	$m_x = E(Y \mid X = x)$
Conditional variance	$\sigma_y^2 = E^2(X \mid Y = y) - E(X \mid Y = y)^2$	$\sigma_x^2 = E^2(Y \mid X = x) - E(Y \mid X = x)^2$
Signal mappings	$f_{x1} : x \to \frac{x}{\sqrt{2}\sigma_y}$ $f_{y1} : y \to \frac{m_y}{\sqrt{2}\sigma_y}$	$f_{x2} : x \to \frac{m_x}{\sqrt{2}\sigma_x}$ $f_{y2} : y \to \frac{y}{\sqrt{2}\sigma_x}$
New signals	$A = E(f_{x1}(X = x))$ $B = E'(f_{y1}(Y = y))$	$A' = E(f_{x2}(X = x))$ $B' = E'(f_{y2}(Y = y))$

If the mapping functions may be assumed to be constant, the partial derivative of NMI with respect to a transformation parameter ϕ is an $O(2n)$ operation:

$$\frac{\partial \mathrm{Y}}{\partial \phi} \cong \left(-\frac{1}{H(E,E')} \right) \frac{2}{n} \sum_{i}^{n} (B_i - A_i) \frac{\partial B_i}{\partial \phi} + \left(\frac{1}{H(E,E')} - \frac{1}{\mathrm{Y}} \right) \frac{2}{n} \sum_{i}^{n} (B_i' - A_i') \frac{\partial B_i'}{\partial \phi} \qquad \ldots(26)$$

3.4 Optimization

Image registration is an optimization task. Cost functions that determine the degree of alignment of the images are either minimized or maximized. Various optimization strategies are applicable in global and local registration. Parameter search methods used in registration include simplex search (Nelder & Mead, 1965), gradient search methods (gradient descent (ascent), Powell's level-set method), 2nd order methods (Levenberg-Marquadt, quasi-Newton, Conjugate Gradient), and genetic algorithm.

In comparing the different optimization strategies, Maes *et al* (1999) found that a two-level multi-resolution strategy using simplex search with conjugate-gradient or Levenberg-Marquadt method was found to be most efficient, outperforming Powell's method by a factor of three. The standard gradient descent approach and quasi-Newton approach were found to be on average less precise than the other methods. However, this comparison was done using PV-interpolation to analytically determine the histogram and histogram derivative. The patterns of interpolation artefacts due to PV-interpolation were evaluated by Pluim *et al.* (2000), who found patterns of local extrema during multi-modal rigid registration. This could explain the poor results of the gradient descent approach found by Maes *et al.*, as gradient descent tends to terminate in local extrema more easily than 2nd order methods.

To improve optimization efficiency, learning rate adaptation (LRA), various weight-initialization methods and optimization methods can be used. To prevent over-fitting, generalization methods like early stopping, pruning and regularization can be used. As

gradient descent (ascent) is used in this project, only tools concerning gradient descent optimization are discussed.

3.4.1 Gradient descent (ascent) and gradient computation

The basic gradient descent (ascent) or steepest descent (ascent) algorithm is used in minimizing (maximizing) the cost function. If the derivative of the cost function with respect to a variable or parameter may be found, to minimize (maximize) the cost function, basically the gradient is subtracted from (added to) the current variable.

For a set of parameters ϕ of length n, and a cost function C, the Jacobian of C with respect to n-dimensional ϕ is:

$$\nabla C = \left(\frac{\partial C}{\partial \phi_1}, \frac{\partial C}{\partial \phi_2}, \frac{\partial C}{\partial \phi_3}, \cdots, \frac{\partial C}{\partial \phi_{n-1}}, \frac{\partial C}{\partial \phi_n} \right) \quad \ldots(27)$$

Using gradient back-propagation technique, the derivative of C with respect to each parameter is the sum of product of partial derivatives:

$$\frac{\partial C}{\partial \phi} = \sum_i^N \frac{\partial C}{\partial g(E_i, E_i')} \left(\nabla \left(g(E_i, E_i') \right) \cdot \frac{\partial T_i(x, y, z)}{\partial \phi} \right) \quad \ldots(28)$$

The equation resembles optical flow from Eq. (5), except for two differences. First, that the Jacobian is taken from a function, $g(E_i, E_i')$ instead of the image (energy) function; second, the transformation vector is used in place of a motion field vector. The function $g(E_i, E_i')$ is a function of the two images and depends on the cost function to be optimized. In the case of NMI found using multivariate Gaussian estimation, Eq. (28) is still directly applicable. In the case of Parzen density estimation,

the relationship between the derivative of *C* and each pixel is not linear as seen in Eq. (18) and Eq. (19). Combining these in the form to look like Eq. (28), the derivative of C may be expressed as the linear sum of the derivative with respect to entropies:

$$\frac{\partial C}{\partial \phi} = k_1 \frac{\partial C}{\partial H(E_i, E_i')} + k_2 \frac{\partial C}{\partial H(E_i')}, \quad k_1, k_2 \in \Re$$
$$\frac{\partial C}{\partial H(E_i, E_i')} = \sum_j \frac{\partial C}{\partial f_j(E_i, E_i')} \sum_i^N \frac{\partial f_j(E_i, E_i')}{\partial g(E_i, E_i')} \left(\nabla(g(E_i, E_i')) \cdot \frac{\partial T_i(x, y, z)}{\partial \phi} \right), \quad \ldots(29)$$
$$\frac{\partial C}{\partial H(E_i')} = \sum_j \frac{\partial C}{\partial f_j(E_i')} \sum_i^N \frac{\partial f_j(E_i')}{\partial g(E_i')} \left(\nabla(g(E_i')) \cdot \frac{\partial T_i(x, y, z)}{\partial \phi} \right)$$

There are two added functions, $f_j(E_i, E_i')$ and $f_j(E_i')$, which are the JPDF and the marginal PDF respectively. By comparing Eq. (28) and Eq. (29), it can be observed that the derivative found using Parzen density estimation is much more complicated and computationally expensive.

The updates to ϕ are a factor dependent on the Jacobian, which is called the update rate or learning rate. In the simplest case, the learning rate, μ, can be assumed to be constant for all ϕ and throughout the optimization process. The process of finding the Jacobian and updating the parameters are repeated until a termination condition is reached. There are many variations to the termination condition, which depends on the Jacobian, or the cost function or some other suitable variable. The pseudo-code of the gradient descent algorithms are found in the appendix.

3.4.2 Learning rate

The choice of learning rate, μ, is an important issue in optimization. A small value would result in slower convergence and may result in the process terminating in local

minima. If μ is large, oscillations may result from the parameters shifting about the global maxima but not nearing it. For gradient ascent in the epoch, *t*, the parameters, ϕ , are updated using the following equation:

$$\phi_i(t+1) = \phi_i(t) + \mu_i \frac{\partial C}{\partial \phi_i(t)} \quad , \quad i = 1, 2, ..., n \qquad \ldots(30)$$

There are also two methods of learning. The first is via batch mode learning, which, as been described before, requires the weights to be updated simultaneously. The other is an online or pattern mode of learning, which updates the weights one at a time. While online mode of learning may prevent termination in local minima and may result in greater computational efficiency, convergence is not guaranteed for pattern mode. Convergence is guaranteed for batch mode learning provided that the learning rate is small enough, albeit the possibility of ending in a local minima.

One way of speeding up learning and by-passing some local minima is to use learning rate adaptation (LRA). While in normal gradient ascent μ is a constant, a separate learning rate that is varied from epoch to epoch is assigned for each parameter, making μ a vector too. There are two forces at work. The first is 'bold driver', which increases the learning rate if the previous search direction is deemed good; the second is 'annealing', which decreases the learning rate to minimize oscillations. Various methods exist, which use different criteria for initializing, increasing and decreasing learning. These include the SuperSAB method (Tollenaere, 1990), the quickprop method (Fahlman, 1988), and the R-prop method (Riedmiller, 1994). In this project we adopt the SuperSAB method, which increases the learning rate if the previous weight updates are in the same direction and vice versa.

3.4.3 Generalization

In optimization problems, generalization refers to how well a trained optimization network performs on unseen examples. This implies that the search space should be smooth, input initialization should be good, the trained data should be sufficiently representative of the entire population, and the network should be powerful enough without memorizing (over-fitting) the training data.

In image registration optimization, smoothness of the search space and input initialization are crucial to achieving good results. In an intrasubject registration, the registration process is the training process, as the parameters are unique to the dataset. Some common ways of providing good generalization are early stopping, network pruning, and regularization. Early stopping is not used in intrasubject registration as there is no separate training process. Network pruning and regularization may be applicable.

The objective of network pruning is to reduce dispensable parameters, thereby reducing computation and preventing over-fitting. The saliency of each parameter measures the indispensability, leaving parameters with low saliency to be neglected. Pruning is usually applied in non-rigid registration rather than rigid registration because of the greater number of parameters. There are several ways of determining saliency. One way is to use the Hessian (eg. Optimal Brain Damage (Le Cun *et al.*, 1990), Optimal Brain Surgeon (Hassibi *et al.*, 1993), etc.), but that is expensive to compute especially in non-rigid registration. The second way is to find the variance of parameters but that is unreliable in registration because registration has comparably

fewer epochs than in a normal non-registration optimization task. The third and easiest way is to base it on the weight (parameter) updates. It has been used together with RBF non-rigid registration (Rohde *et al.*, 2003), whereby the gradient magnitude for each RBF is used to determine the saliency.

Regularization, also known as smoothing, addresses over-fitting by reducing the power of the optimization network. In image registration, it may be introduced as a penalty term to counter the cost function so that the image is spatially smooth. Denoting N as the number of image samples and T as the entire transformation matrix, the regularization cost function may be expressed as:

$$C_{\mathrm{Re}g} = \frac{1}{N}\int_0^X \int_0^Y \int_0^Z \nabla \cdot \nabla\big(T(x,y,z)\big)\,dz\,dy\,dx \qquad \ldots(31)$$

Combined with regularization with NMI (that is to be maximized), the overall cost function to be maximized will be:

$$C = \mathrm{Y} - \lambda C_{\mathrm{Re}g} \qquad \ldots(32)$$

where λ is a constant that determines the amount of smoothness required. Experimentally, $\lambda \in [0.01, 0.05]$ was found to be suitable.

Adding some small amount of random noise to the parameters may also perturb the overall function from a local minimum without moving it significantly away from the global maxima. Spatially, some smoothing may be applied to all transformation coordinates to create this perturbation. Though it is not random, but it makes more sense because the perturbation results in the overall transformation becoming smoother.

CHAPTER FOUR

IMPLEMENTATION

4.1 Overview of registration

The overall registration process consists of three steps as illustrated in Figure 4.1. The first is pre-registration, where the dataset specifications are understood prior to pre-processing the dataset so that registration can be done efficiently and effectively. The next step is registration proper, which consists of global motion modeling (rigid registration) and local motion modeling (non-rigid registration). The final step is to analyze the registration results and to compare registration results against non-registered ones in detecting lesions.

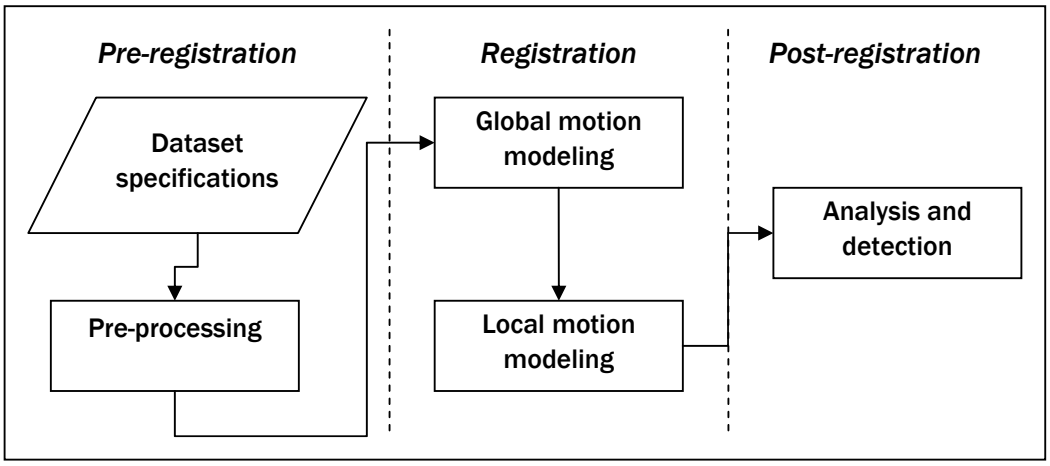

Figure 4.1: Flowchart of registration process.

Using the standard medical image registration classification criteria proposed by Maintz and Viergever (1998), registration paradigm used in this project is summarized in Table 4.1.

Table 4.1: Registration Overview.

Criteria	CE-MRI
Dimensionality	3-D to 3-D registration, but analysis is done serially.
Nature of registration basis	Intrinsic (volume-based registration), using NMI estimated with Parzen density estimation or with multivariate Gaussian estimation.
Nature of transformation	Rigid and non-rigid (curved) in IR^3. Rigid registration includes rotation and translation (6 degrees of freedom). Non-rigid registration uses trifocal 3rd-order B-splines.
Domain of transformation	Global (rigid) and local (non-rigid). Local modeling implemented in multi-resolution fashion.
Interaction	Registration is automatic. Initial segmentation of breast may be manually done.
Optimization procedure	Gradient ascent, with learning-rate adaptation, network pruning, and regularization.
Modalities involved	Monomodal, but it includes non-uniform intensity change due to the contrast-agent.
Subject	Intrasubject.
Object	Breast(s); each side to be registered individually.

4.2 System overview

4.2.1 Dataset and imaging protocol

Prior to pre-processing and registration, the specifications of the dataset have to be known. The MR mammogram datasets were obtained from the Diagnostic Imaging Department in the National University Hospital of Singapore. Each CE-MRI dataset contains a series of five 3-D scans, each scan having the typical specifications below:

- Size: 256x256x24 voxels
- Dimension: 1.05mm x 1.05mm x 5.45mm
- Orientation and object: Entire chest section in axial view
- Format: E-Film (16-bit)
- Intensity Range: 0 to 255
- MRI Equipment: GE Signa 1.5T
- Pulse Sequence: 3-D Fast spoiled gradient echo, no spectral fat suppression
- TR = 25.6ms, TE=3ms (fractional echo)

- Flip angle = 30^{o}, FOV = 32 to 40cm
- Contrast Agent: Gadolinium-pentetate Gd-DTPA (MagneVist) 0.2mmol/kg

Variations to this protocol are mainly in the number of slices, which can vary from 16 to 56 depending on the volume size to be acquired. The contrast agent is injected after the first scan, and post-contrast scans will follow in the next 5 to 20 minutes. Each 3-D scan requires 30-60 seconds of acquisition time, again depending on the number of slices.

4.2.2 Pre-processing

Prior to registration, the regions of interest will have to be segmented from the entire CE-MRI scans. This is to minimize the regions of interest outside the breasts, since these do not serve as useful landmarks for registration. It is thus convenient to segment each breast separately and also to register each breast separately. This will reduce the data size, and will provide better optimization of parameters since the free-form motion of the breasts can be considered to be largely independent. Most authors in non-rigid registration of CE-MRI have advocated separate registration for each breast (Hayton *et al.*, 1997; Hayton *et al.*, 1999; Fischer *et al.*, 1999; Reichenbach *et al.*, 2002). It is not clear whether Rueckert *et al.* (1999) registered each breast separately.

The next issue in pre-processing is whether the breast should be automatically segmented. Ideally it should be so because it would be extremely tedious to manually segment each dataset, given the high multi-dimensionality (3-D series). Hayton *et al.* (1997) presented a morphological method with graph search for edges to obtain the breast profiles for each scan that was shown to derive good segmentation estimates of

the breast. This method was deemed unsuitable in this project for several reasons: (i) the high variance of amount of fat (higher intensity) required for good segmentation of the breast (from external regions and from the lungs); (ii) variability of histopathology of patients; and (iii) presence of magnetic gradient bias that create non-uniform illumination in different slices.

A much simpler and intuitive method is to make use of basic features in the axial MRI acquisition. As the chest wall of subjects in the upper-torso regions are largely perpendicular and parallel to the slices and axial direction respectively, a 2-D segmentation in the slice plane with the largest cross-sectional area of the breast can be used as a guide. A better method would be to perform a maximum intensity projection (MIP) in the axial direction. This will result in a 2-D output that resembles all the slices in a 3-D scan (Figure 4.2). The breast region can be easily manually segmented in the 2-D plane by using the same segmentation mask across all planes to encompass the entire breast volume. This method will also reduce the non-uniform illumination effects of magnetic gradient-bias.

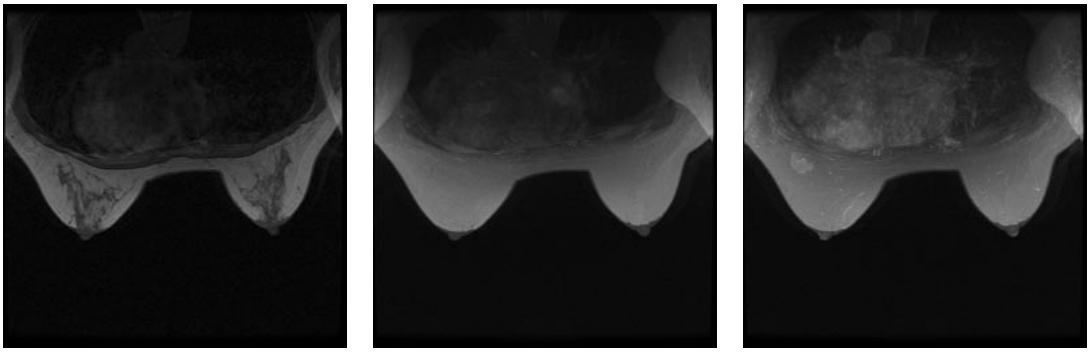

(a) (b) (c)

Figure 4.2: Comparing MIPs of breast volume. (a) A slice taken from 3-D MRI pre-contrast scan, (b) MIP of pre-contrast scan in axial direction, (c) MIP of a post-contrast scan. With motion constrained within the breast coil, automatic/manual segmentation using a MIP from any part of the sequence can be used for the entire series.

To create an automatic method for segmentation based on the MIP, threshold the MIP image followed by contour-tracking to detect the bounding box for the breast. However, comparisons between manual and automatic segmentation tend to favor manual segmentation for several reasons: (i) the region-of-interest for registration sometimes may not be required to cover the entire breast; (ii) the MIP image can be easily manually segmented; (iii) breast intensities can vary significantly from patient to patient; (iv) wrap-around effect during to sampling aliasing, as can be seen in Figure 4.2; and (v) 'ghost' aliasing effect due to patient movement during acquisition.

Thus the object for registration is a manually segmented breast volume.

4.2.3 Global motion model

Rigid transformation is chosen to model global motion. It has 6 degrees of freedom, thus requiring fewer parameters to optimize compared to general affine transformation, which has 12 degrees of freedom. Rueckert *et al.* (1999) observed that affine registration was only marginally superior to rigid transformation. In addition, scaling should be minimal because the volume of the breast can be considered to be constant during the short scanning time. Any minute scaling may be modeled during the non-rigid registration phase.

Due to the non-uniform change in intensity, NMI is used as the cost function. While Maes *et al.* (1999) reported poorer results using the gradient descent approach as compared to several other optimization approaches, it was precisely this approach that had also been used with success in other CE-MRI registration attempts (Rueckert *et al.*,

1999). Mae's comparison was done using PV-interpolation, which suffered from interpolation artefacts (Pluim *et al.*, 2000). This project uses density estimation (Parzen density estimation, multivariate Gaussian estimation) that has higher order of interpolation, and will theoretically have fewer interpolation artefacts. The gradient descent (ascent) optimization is chosen for its faster convergence (than simplex or Powell's set method) and its smaller computational load (than 2nd order methods).

NMI will be at its maximum when the images are aligned, so the search direction is an ascent. The terminating conditions are based on two factors. First, if the Euclidean sum of the Jacobian was smaller than a small fraction, ε, of its initial value – which will indicate reaching a plateau in the search space; or secondly if the number of epochs exceeded η. Experimentally, it was found that using $\varepsilon = 0.02$ and $\eta = 15$ was sufficient to attain convergence effectively.

To obtain the derivative of the cost function following Eq. (28) or Eq. (29), the only partial derivative that is different between rigid and non-rigid registration is $\frac{\partial T(x, y, z)}{\partial \phi}$. In rigid registration, finding this derivative is trivial as it can be computed directly from Eq. (1).

To examine the effects of learning rate adaptation (LRA) using the SuperSAB method (Tollenaere, 1990), a comparison was made between 10 representative datasets. Figure 4.3 shows a typical learning curve in NMI rigid registration. With an acceleration ('bold driver') rate of 1.2 and deceleration ('annealing') rate of 0.5, the optimization progress tends to be faster due to the acceleration, and yet more stable due to the decelerating effects on oscillating parameters. NMI found with using LRA is on

average 2.1% (between -1.0% and 4.8%)[7] higher than without using LRA. This shows that using LRA in rigid registration attains better optimization.

As there are only 6 degrees of freedom in rigid registration, network pruning is not used. Regularization is not applied because rigid transformations are smooth. A single resolution (at the highest) is preferred to multi-resolution for two reasons: (i) the motion between the images is fairly minute (estimating the optical flow global motion vectors to be within a pixel width); and (ii) local shifts will be accounted for in multi-resolution non-rigid registration.

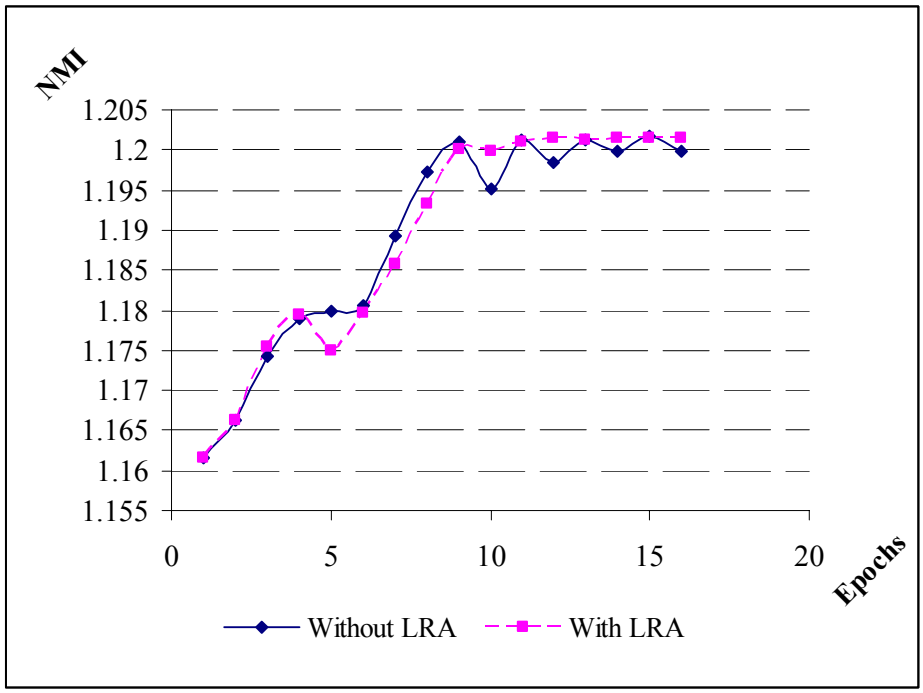

Figure 4.3: Comparing a typical optimization progress with and without learning rate adaptation (LRA). Faster convergence can be seen in the initial epochs (1-5) albeit a larger fallout (5), but LRA recovery is better because of fluctuating parameters are de-emphasized, resulting in lower oscillations (10-15).

[7] Computed as a percentage of the amount of increase in NMI for the entire rigid registration process (without using LRA).

The rigid registration algorithm is summarized in Figure 4.4.

initialize the rigid parameters ϕ, the epoch count, *t*, the LRA learning rates, μ, the accelerating rate, ω_+ and the decelerating rate, ω_-

calculate the gradient vector of $C = C_{NMI}$, ∇C

while $\left(\|\nabla C\| > \varepsilon\right)$ AND $\left(t < \eta\right)$ **do**

increase *t* by 1

recalculate the parameters $\phi_i(t) = \phi_i(t) + \mu_i \dfrac{\partial C}{\partial \phi_i(t-1)}, \quad i = 1,2,3,4,5,6$

recalculate the gradient vector, ∇C

for all *i*

if $\left(\dfrac{\partial C}{\partial \phi_i(t-1)} \times \dfrac{\partial C}{\partial \phi_i(t)}\right) > 0$ **then** $\mu_i = \mu_i \times \omega_+$

else if $\left(\dfrac{\partial C}{\partial \phi_i(t-1)} \times \dfrac{\partial C}{\partial \phi_i(t)}\right) < 0$ **then** $\mu_i = \mu_i \times \omega_-$

Figure 4.4: The rigid registration algorithm

4.2.4 Local motion model

Hierarchical B-splines mesh is used to model local motion because it can be easily used in a multi-resolution fashion. This approach of using an evenly spaced is preferred to using RBFs or point-based splines because there are no obvious landmarks in CE-MRI that can be used as positions of reference. In an $\mathbb{R}^3$ B-spline mesh, each control point has 3 degrees of freedom; a 128x128x24 volume at the finest resolution the entire mesh will have in excess of a million degrees of freedom.

In order to maximize efficiency and to provide better initialization of parameters a multi-resolution approach to implementing B-spline model is used. At each level the mesh interval is halved and the sampling resolution is doubled. It was found that using a minimum of four levels (including the highest resolution) was computationally

efficient and gave good results. Figure 4.5 shows how a typical registration progresses with the different stages.

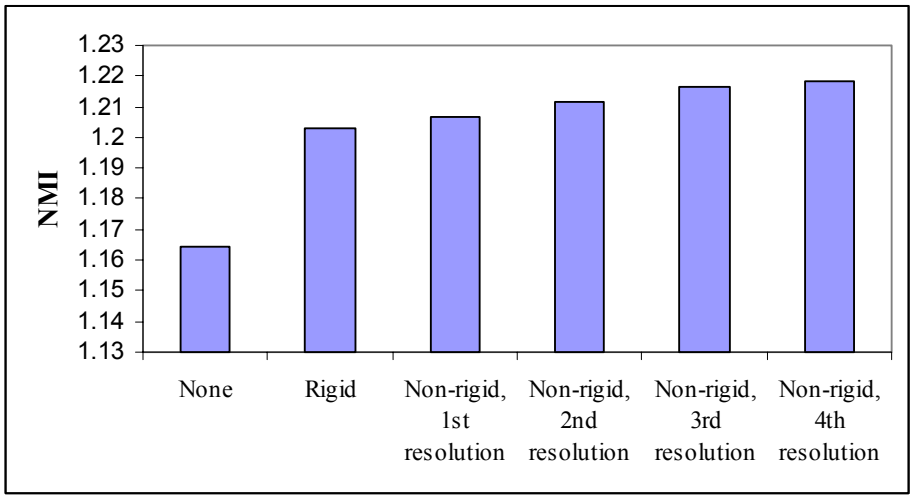

Figure 4.5: Typical progress of NMI in the progressive stages of registration.

NMI is the chosen cost function, optimized using gradient ascent. Simplex search and Powell's set method are inappropriate because of the high computational costs of NMI, while 2^{nd}-order methods are also inappropriate because the large number of degrees of freedom ($\sim 10^6$) will make Hessian computation expensive. This also rules out using network pruning methods that require the Hessian. Online weights update will also be ineffective because of the high computational costs of NMI and its analytical gradient. Thus, all control points will be simultaneously updated.

Another advantage of simultaneously updating the parameters of a regular mesh like B-splines is that the derivative of the B-splines trifocal tensor with respect to a shift in a control point is the same for all control points; this derivative will only need to be computed once and applied to all control points using convolution. Following Eq. (2), the derivative of transformed coordinates is simply:

$$\frac{\partial T(x,y,z)}{\partial \phi_{i+l,j+m,k+n}} = \begin{cases} B_l(u)B_m(v)B_n(w) & , \quad T(x,y,z) \subseteq \phi_{i+l,j+m,k+n} \\ 0 & , \quad otherwise \end{cases} \qquad \ldots(33)$$

Since *i, j*, and *k* are the normalized indexes inside a regular B-Spline grid, the derivative for every interval $(\delta_x, \delta_y, \delta_z)$ is the same. Thus there will be computational savings when the derivative is found using convolution.

The terminating conditions are dependent on the value of the cost function rather than on the Jacobian for several reasons: (i) non-rigid registration has more local extrema than rigid registration; (ii) under-fitting can be accommodated in a multi-resolution strategy, but over-fitting would result in early termination in local extrema. Regularization as defined in Eq. (31) was added to the cost function in Eq. (32). In addition to this, some additional smoothing is applied to each coordinate at the end of each epoch. The purpose of this smoothing is to perturb the coordinates so as to prevent the optimization from terminating in local extrema. This perturbation also makes sense because it makes the overall transformation smoother. A comparison over 10 representative datasets showed less fluctuation in the learning curves, and consistently higher NMI values (-0.3% to 3.2%, taken as a percentage of total increase in NMI for each resolution).

Though LRA is good for rigid registration, it is not always good for non-rigid registration. Due to the multi-resolution strategy adopted, over-fitting at a lower resolution often results in smaller improvements and earlier termination at a higher resolution. Applying LRA will also defeat the purpose of segmentation when

registering using multivariate Gaussian estimation (see chapter 5). Thus LRA is not employed in the non-rigid phases of registration.

The non-rigid registration algorithm is summarized in Figure 4.6.

initialize the control point resolution and image resolution
repeat
  initialize the non-rigid parameters ϕ, and the epoch count, *t,* constant learning rate, μ, and regularization constant, λ
  calculate the gradient vector of $C = C_{NMI} - \lambda C_{\mathrm{Re}g}$, ∇C, and NMI, $\mathrm{Y}(t)$
  while $\mathrm{Y}(t) - \mathrm{Y}(t-1) > \varepsilon, \quad \varepsilon \in \Re^{+}$ **do**
    increase *t* by 1
    recalculate the parameters $\phi_i(t) = \phi_i(t-1) + \mu \dfrac{\partial C}{\partial \phi_i(t-1)}, \quad i \in [1, n]$
    smooth all coordinates, $T(x, y, z, t) = T(x, y, z, t-1) - \lambda \nabla \cdot \nabla (T(x, y, z, t-1))$
    recalculate the gradient vector, ∇C
  increase the control point resolution and image resolution
until finest level of resolution is reached

Figure 4.6: The multi-resolution, non-rigid registration algorithm.

4.2.5 Detection

Using a variation of the thoroughly tested 3TP method proposed by Degani *et al.*, (1997), and the more graduated system defined by Baum *et al.* (2002), a more robust and simpler scoring system based on intensity factors alone (initial enhancement and post-initial enhancement) is shown in Table 4.2. To illustrate how initial and postinitial enhancements ω_1 and ω_2 would be calculated in Figure 4.7 signal A (normal tissue)

has $\omega_1 = 10.9\%, \omega_2 = 8.7\%$, signal B (benign lesion) has $\omega_1 = 66.7\%, \omega_2 = 13.5\%$, and signal C (malignant lesion) has $\omega_1 = 200\%, \omega_2 = -16.7\%$.

Table 4.2: A simple and robust scoring system.

	None (Score = 0)	Benign (Score = 1)	Malignant (Score = 2)
Conditions:	$(\omega_1 \le \kappa_1)$	$(\omega_1 > \kappa_1)$ AND $(\omega_2 > \kappa_2)$	$(\omega_1 > \kappa_1)$ AND $(\omega_3 \le \kappa_2)$
Definitions:	$\omega_1 = \frac{\max(I_2, I_1) - I_0}{I_0} \times 100\%$, $\omega_2 = \frac{\min(I_3, I_4) - \max(I_1, I_2)}{\max(I_1, I_2)} \times 100\%$, $\kappa_1 \in [30\%, 200\%]$, $\kappa_2 \in [-20\%, 50\%]$ Default: $\kappa_1 = 60\%, \kappa_2 = 0\%$		

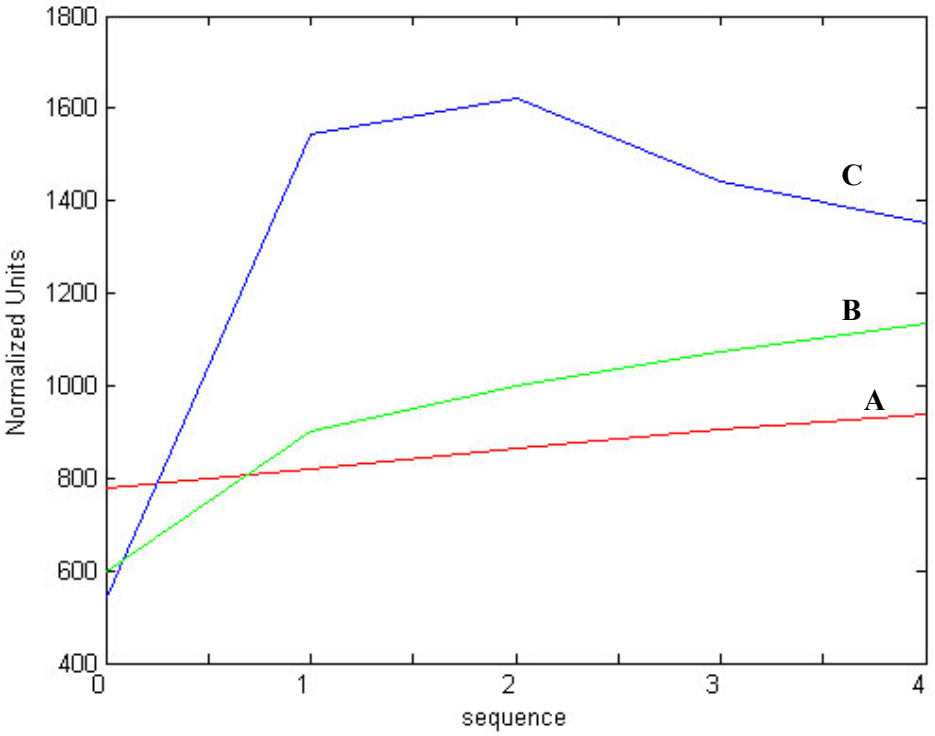

Figure 4.7: Typical signal enhancements in CE-MRI, for normal tissue (A), benign lesions (B), and malignant lesions (C).

This method is based on 5 time scans (1 pre- and 4 post-contrast). The first time point is taken as the maximum intensity between the 1st and 2nd post-contrast scan; the

second time point is taken as the minimum intensity between the 3rd and final post-contrast scan. By using the maximum and minimum conditions and applying it voxel by voxel, this scoring system is more sensitive to variations in contrast-enhancement dynamics. The initial enhancement (wash-in) and post-initial enhancement (wash-out) constants κ_1, κ_2 are interactively changed depending on the perceived size of the lesions to be detected, thus making it robust to blurring artefacts. In addition, wider ranges of values are allowed for κ_1 and κ_2 because the discriminating characteristic for malignancy with the GE scanner used in this project tends to be a significantly high (greater than 100%) wash-in rather than a fast wash-out. For example, signals with $\omega_1 = 180\%, \omega_2 = 5.0\%$ do not have the wash-out characteristic, but the strong initial enhancement is strongly indicative of malignancy. Therefore, a voxel which continues to retain a score of 1 when κ_1 is increased from the default of 60% to 180% should really be considered to be malignant.

4.2 System implementation

4.2.1 System platform

The registration algorithm is implemented in Visual C and C++ for efficiency. All visualization is done using OpenGL v1.0. The registration software is run using a Pentium IV 2.4MHz system with 512MB DDR RAM.

4.2.2 Program organization and work-flow

The program is organized into two layers (Figure 4.8). The graphical user interface (GUI) layer is divided into the dataset manager and the registration GUI. The dataset manager allows the user to preview and select the desired dataset for registration, review or analysis. Each dataset consists of several types of data. First, there is the set

of original CE-MRI stored in DICOM format. There are also datasets of segmented and registered images stored in a matrix format used in this project. This format stores image intensities in 32-bit floating point. Next, there are motion field vectors that are also stored in the matrix format, used for one of the display functions. Lastly there is a configuration (*.ini) file that is used to integrate all the data. Each dataset is stored in separate folders, bearing the same name as the configuration file.

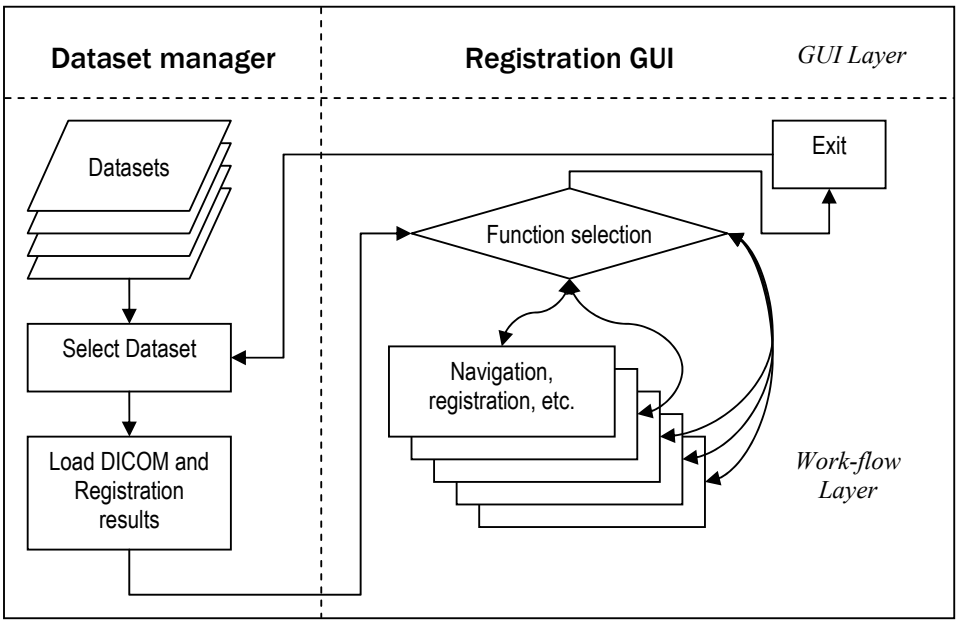

Figure 4.8: System work-flow and organization.

After a dataset is selected, the registration GUI and the original data are displayed. The functions are available in the button panel and in the menu. A brief image description and mouse-pointer intensity values are displayed in the status bar. The study list shows a list of available matrices (studies) that can be selected for viewing, editing, and registration.

Screen-shots of both GUIs are found in Figures 4.9 and 4.10.

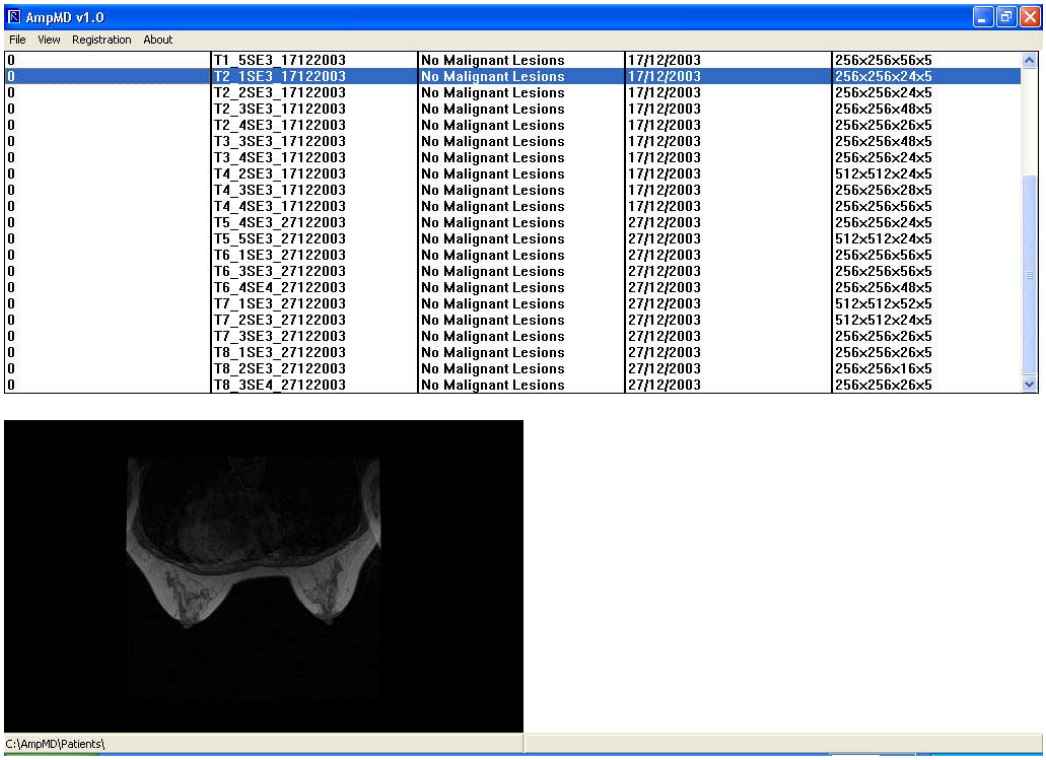

(a)

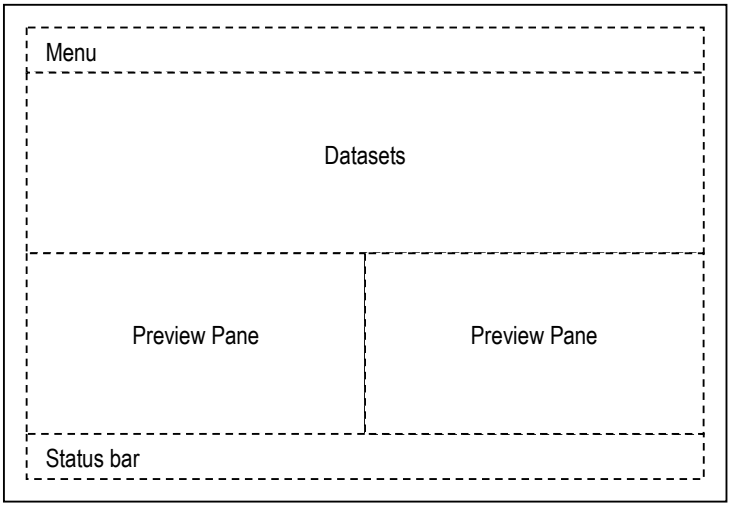

(b)

Figure 4.9: Dataset manager GUI. (a) Screen-shot, and (b) Layout description

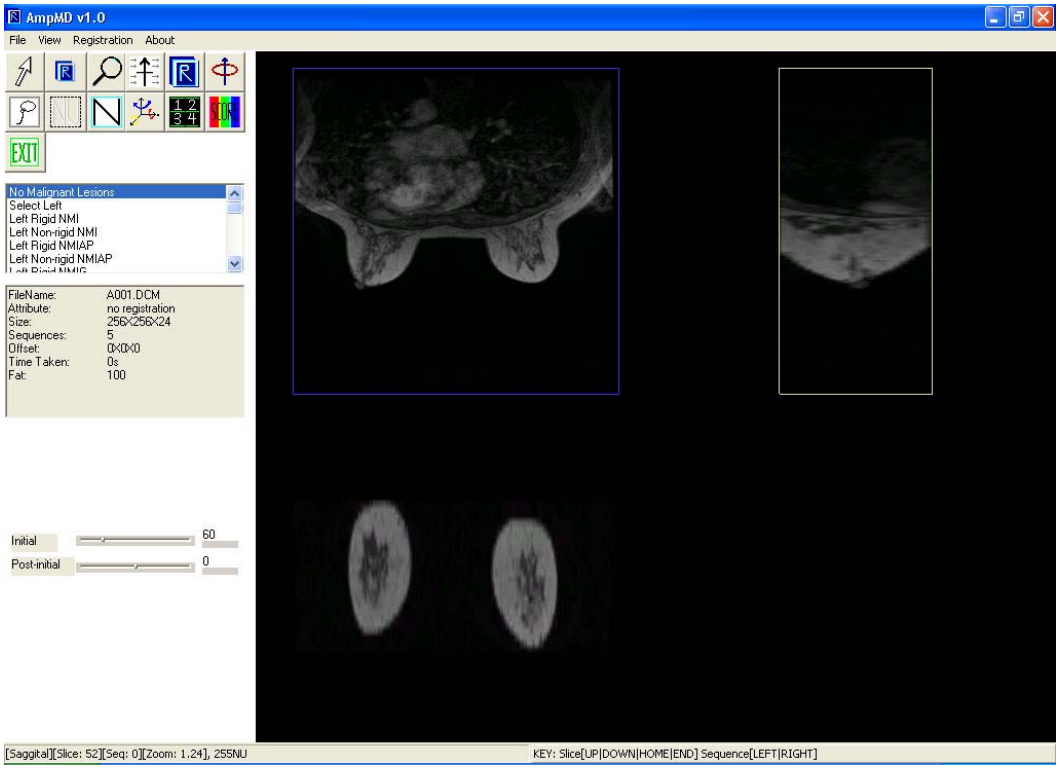

(a)

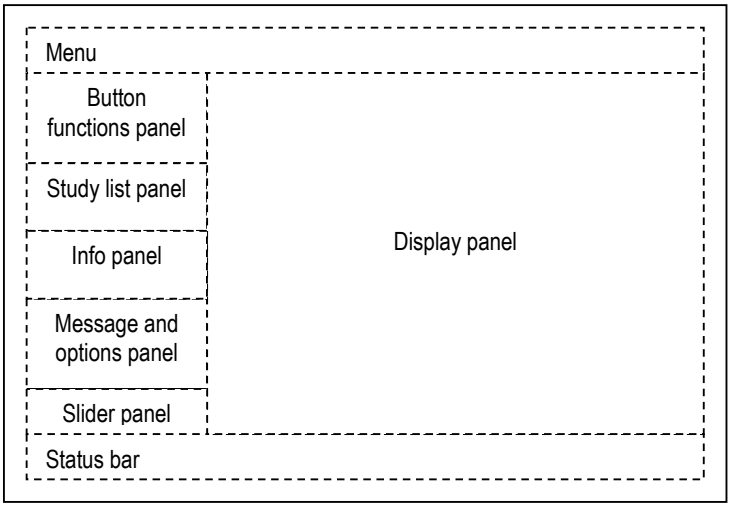

(b)

Figure 4.10: Registration GUI. (a) Screen-shot, and (b) Layout description.

4.2.3 Functions

The functions of the program are grouped by their locations. Most functions are activated from the registration GUI.

- *Menu*: There are three main menus. “File” functions are used in both GUIs for importing new images, saving images, screen-shots and opening the dataset. “View” functions are used for changing the layout in the display panel. “Registration” functions are used for configuring the resolutions and optimization cost functions used in registration.
- *Button functions panel*: These are the main functions used in the registration GUI. A summary of the buttons are listed in Table 4.3.
- *Study list panel*: This panel displays the studies found in the selected dataset, and allows the user to change the displayed study. For multiple-study display, selection will be disabled in this panel.
- *Info panel*: This panel shows the study information of the current study selected.
- *Message and options panel*: This panel displays messages and options when user decision is required.
- *Slider panel*: This allows the user to manually select values for certain variables, particularly the initial and postinitial enhancements constants.
- *Status bar*: The left status bar displays the view type, slice number, sequence number, zoom factor, and the pointer intensity. The right status bar displays the mouse and keyboard commands for the button functions selected.
- *Display panel*: There are many user-interaction functions that are activated in the display panel, depending on the functions that had been activated. These range from study selection, change of view, etc.

Table 4.3: List of functions in button functions panel.

Function	Description
Panning	Allows the user to pan the image on the display panel.
Zooming	Allows the user to zoom in and out on the image on the display panel.
Contrast and brightness	Allows the user to adjust the contrast and brightness using the mouse.
Navigation	In single study view, this allows the user to navigate in slice and sequence within the same study. In multiple study view, this allows the user to navigate between studies as well.
Rotate view	Rotates between axial, saggital and coronal views.
Change view type	Cycles between options for normal, difference and maximum intensity projection (MIP) views. User will confirm the option by pressing the enter key.
Free-form ROI selection	Allows the user to interactively select the ROI on the display panel.
Registration	Starts the registration process on the current study.
Motion field vector display	Toggles the display of motion field vectors on registered datasets.
Multiple view display	Toggles between single and multiple study view.
Score display	Toggles the display of color-coded scoring.
Exit	Exits program.

4.2.4 Analyzing registration results

The functions and their layout and interactivity are specially designed to aid the clinical user to register the images and to analyze the registration results within studies and against different studies. The main objective of this program is to compare registration results against non-registered or registered results derived using different optimization schemes. The best way to do this is to use the multiple-study view with difference (and normal) images with motion field vectors and scoring as shown in Figure 4.11. The difference images for no registration, rigid registration and non-rigid registration can be compared simultaneously. The clinician can toggle the motion field vectors to observe the optimum motion fields found by the registration schemes. The scoring display can be toggled on or off to observe the 3TP analysis or the difference gray-scale respectively.

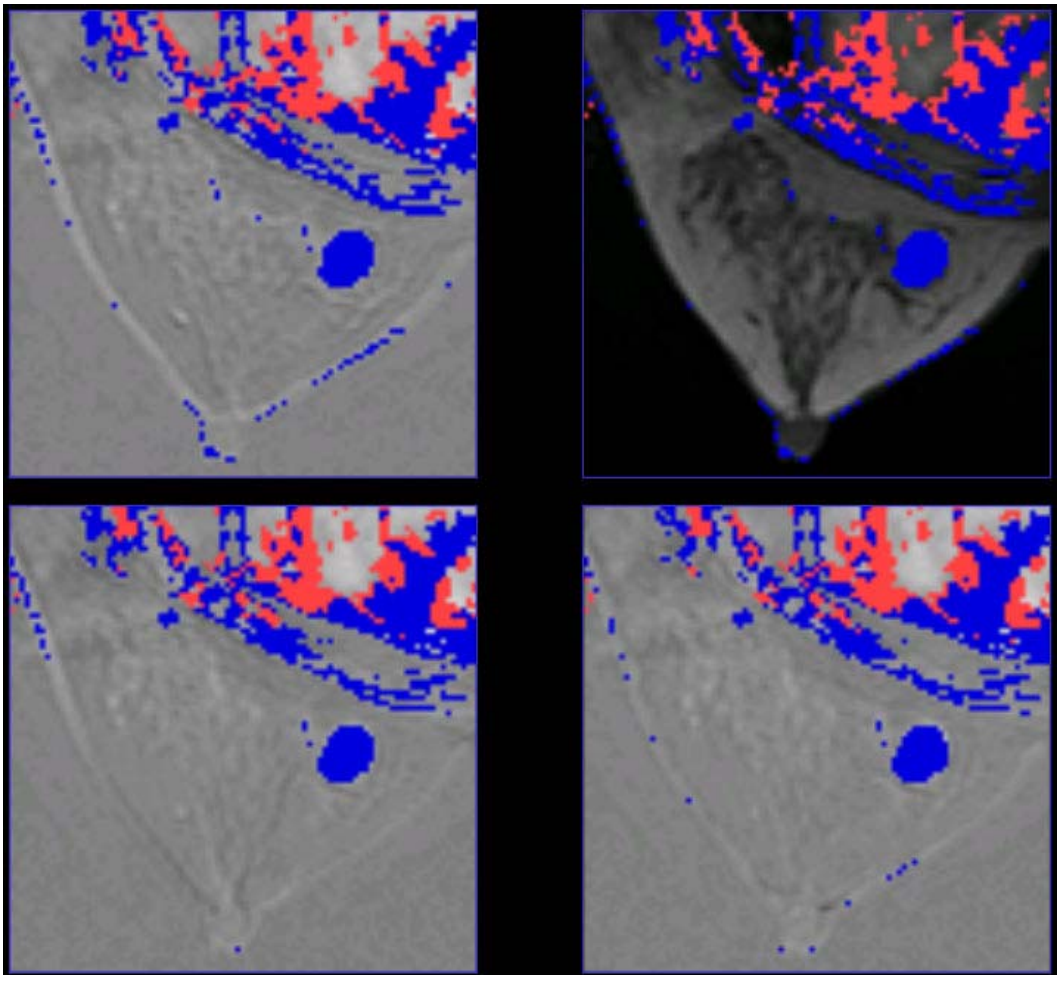

Figure 4.11: Display panel showing multiple-study view for user to compare scoring results.

Also, by adjusting the initial and postinitial enhancement constants κ_1, κ_2 in the slider panel, the scoring display will change accordingly to the desired display requirements. This will be particularly useful to detect lesions of different sizes. Figure 4.12 shows how the scoring would differ when κ_1 was changed from 50% to 100% (decrease in sensitivity). So even though the lesion area is colored blue, the lesion is suspiciously malignant because of the high initial enhancements above 100%.

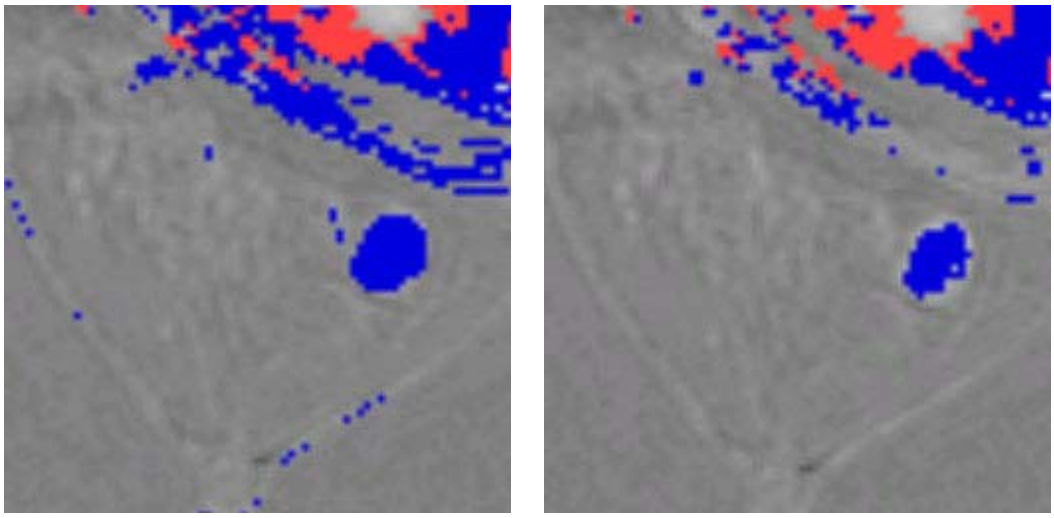

(a) (b)

Figure 4.12: Difference images with scoring at different enhancement constants. (a) $\kappa_1 = 50\%$ (high sensitivity to lesions), and (b) $\kappa_1 = 100\%$ (low sensitivity to lesions). Highlighted regions indicate lesions found using the 3TP method. Blue indicates fast wash-in, red indicates fast wash-out.

CHAPTER FIVE

NEW MODEL OF CONTRAST ENHANCEMENT

In section 3.3.3, multivariate Gaussian estimation was introduced as a method of estimating NMI so as to simplify the calculation of the NMI derivative. This required all conditional PDFs to be Gaussian. Using an intuitive model of contrast enhancement for CE-MRI, it will be shown that registration of CE-MRI is a special case where multivariate Gaussian estimation is applicable, provided that hypervascularized regions are excluded from the optimization process during non-rigid registration.

5.1 Modeling contrast enhancement

In registration, the pre-contrast scan is used as the reference volume, and any of the post-contrast scans is the registered volume. The model proposes to separate the motion variables from the non-uniform change in intensity due to the contrast agent. If the variables can be isolated, then registration of the motion (global and local) can be made independent of the changes due to the contrast agent. Figure 5.1 illustrates this model, which uses an approximation of the reference and registered volumes to separate motion variables from the non-uniform change in intensity.

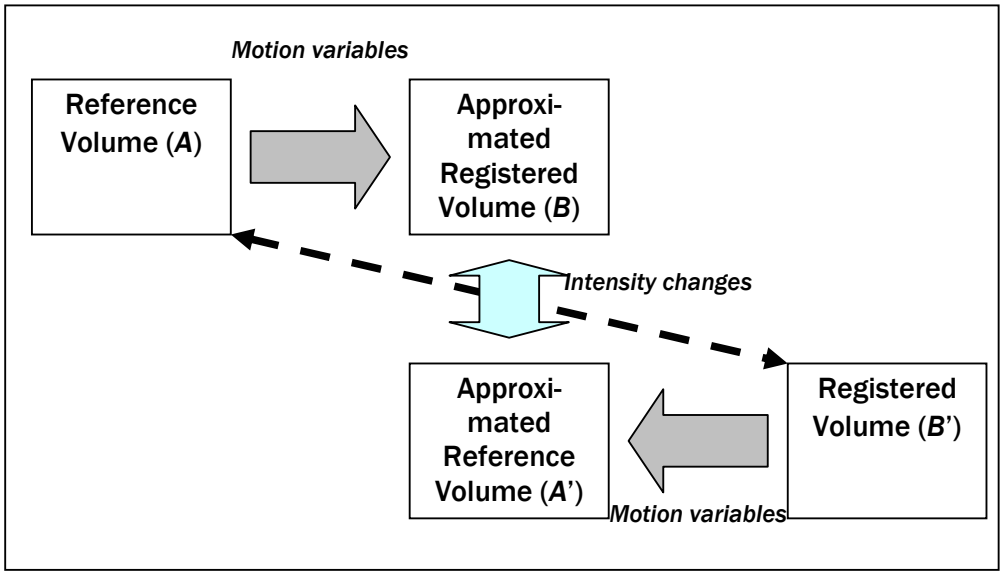

Figure 5.1: Theoretical model of contrast enhancement behind applying multivariate Gaussian estimation to CE-MRI registration.

MRI has good resolution in tissue, so different intensities in the reference volume can indicate the type of tissue. However contrast-enhancement dynamics can be complicated, and uptake rate of the contrast agent is non-linearly related to the intensity value in MRI. The task involved in CE-MRI is to find lesions, and if found, determine malignancy. This model proposes that tissue may be classified as non-hypervascularized (non-lesions) or hypervascularized (lesions), with each having a distinct intensity distribution. By separating the two classes, simplifications to the existing registration paradigm may be made to speed up registration and improve the quality of registration.

Assumptions: Since most tissues found in the breast, even enhancing areas, are non-lesions, so the dominant distribution will belong to non-lesions. So two further assumptions are made about the main distribution:

1. Contrast-enhanced dynamics can be modeled as a Gaussian distribution;
2. Motion artefacts can also be modeled as a Gaussian distribution.

When both assumptions are combined, the net effect will also be Gaussian. Assuming that lesions can either be neglected or removed, a suitable method for implementing this model was implemented.

5.2 Applying multivariate Gaussian estimation

To integrate the model with registration, multivariate Gaussian estimation of the conditional PDFs can be used. From Eq. (26), the derivative of NMI found using multivariate Gaussian estimation can be divided as a sum of two terms:

$$\frac{\partial \mathrm{Y}}{\partial \phi} \cong \frac{\partial \mathrm{Y}_1}{\partial \phi} + \frac{\partial \mathrm{Y}_2}{\partial \phi}$$

$$\frac{\partial \mathrm{Y}_1}{\partial \phi} = \left(-\frac{1}{H(E,E')} \right) \frac{2}{n} \sum_i^n (B_i - A_i) \frac{\partial B_i}{\partial \phi} \qquad \text{(Registered volume approximation)}$$

$$\frac{\partial \mathrm{Y}_2}{\partial \phi} = \left(\frac{1}{H(E,E')} - \frac{1}{\mathrm{Y}} \right) \frac{2}{n} \sum_i^n (B'_i - A'_i) \frac{\partial B'_i}{\partial \phi} \qquad \text{(Reference volume approximation)}$$

The first term is called ‘registered volume approximation’ while the second is called ‘reference volume approximation’. The first term approximates the registered volume B from the actual registered volume E' by assuming that no contrast agent has been injected. Similarly, the second term approximates the reference volume A' from the actual reference volume E by assuming that the same amount of contrast agent has been present in both E and E'. If the only difference between B and A' is non-uniform intensity changes due to the contrast agent, then the model’s assumptions will be met.

As proven in section 3.3.3, multivariate Gaussian estimation will be good if and only if the conditional PDFs are perfectly Gaussian. It may be even better than Parzen density estimation in terms of registration quality.

In general, the conditional PDFs in this registration task are not Gaussian. Figures 5.2 and 5.3 show the un-registered conditional PDFs, $P(E'|E, X = x)$ and $P(E|E', Y = y)$ respectively. These conditional PDFs depict intensities of particular interest (intensities corresponding to tissue) and are representative of the datasets examined. Both conditional PDFs show bell-shaped distributions, but are not perfectly bell-shaped. The 'forward looking' PDF $P(E'|E, X = x)$ in Figure 5.2 has a dominant bell-shaped distribution and an outlier distribution. It is observed that both distributions appear to shift to the right with time, and that the outlier distribution becomes more distinct with time. This is consistent with the observations of intensity enhancement in normal tissue (dominant distribution) and lesions (outlier distribution). The 'retrospective' PDF $P(E|E', Y = y)$ in Figure 5.3 also has bell-shaped distributions that appear to shift to the left with time. Outliers to the right of the distribution can be considered to be artefacts as intensity should increase from pre- to post-contrast scans; contributions from the left of the distribution are due to contrast enhancement from normal tissue and lesions.

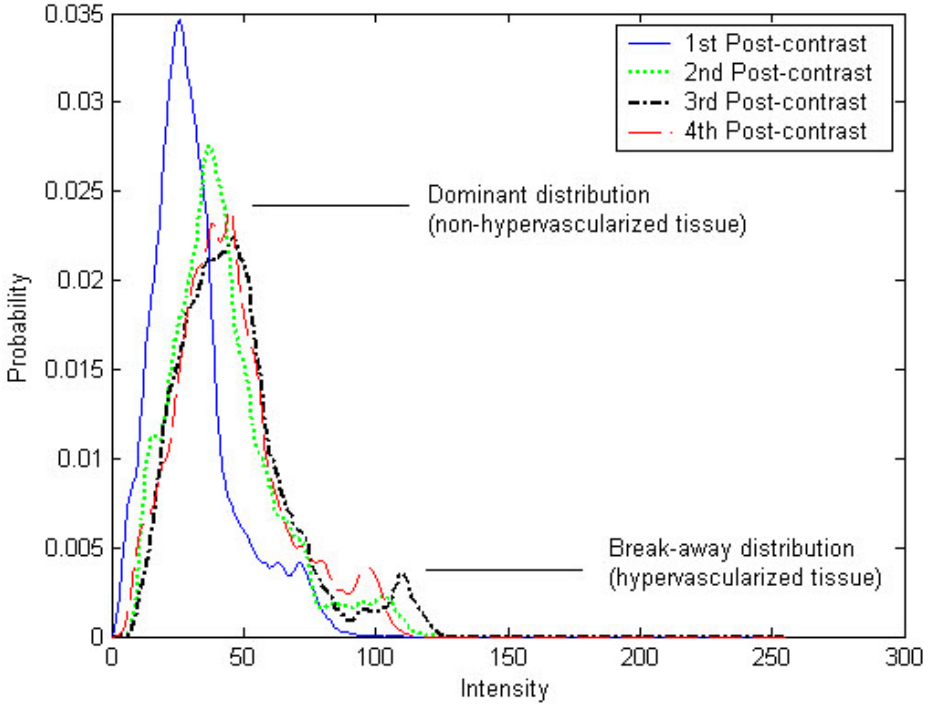

Figure 5.2: Conditional PDFs $P(E'|E, X = 35)$, for a set of four post- to pre-contrast registration, demonstrating the net increase in the predominant distribution mean, as well as the emergence of a break-away distribution that corresponded to hypervascularized tissue.

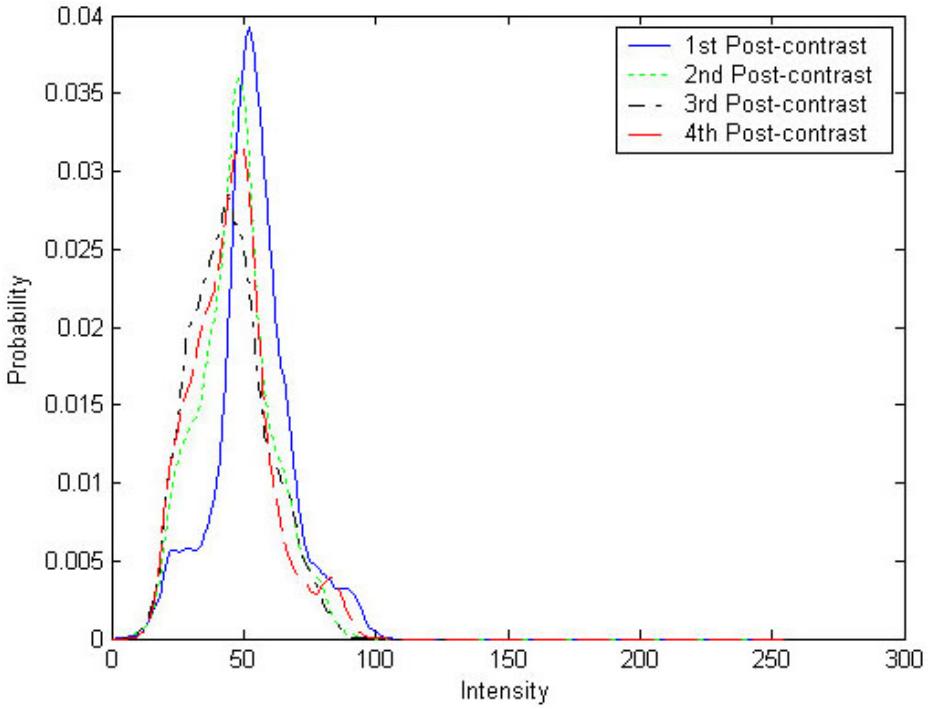

Figure 5.3: Conditional PDFs $P(E|E', Y = 50)$, for a set of four post- to pre-contrast registration. While the effects of the contrast-agent were not as obvious, the retrospective effects could be correlated to the other effect observed in $P(E'|E, X = x)$.

Comparing 'forward looking' $P(E'|E, X = x)$ with its estimated Gaussian in Figure 5.4 it can be seen that the peaks roughly coincide, but the outlier distribution stands out. The estimated variance will be larger mainly because of the outlier distribution. The amount of probability error was 0.00203 (see Table 5.3 for a detailed comparison), which was about a tenth of the peak probability in the estimated Gaussian. In normalizing this probability error against the peak probability in the estimated Gaussian distribution, the estimation error across 10 datasets had the range of [7.7%, 15.2%] and the mean of 10.1%. While the error can be considered small, it is not ideal. For now, the effects of the outlier distribution may be assumed to be negligible.

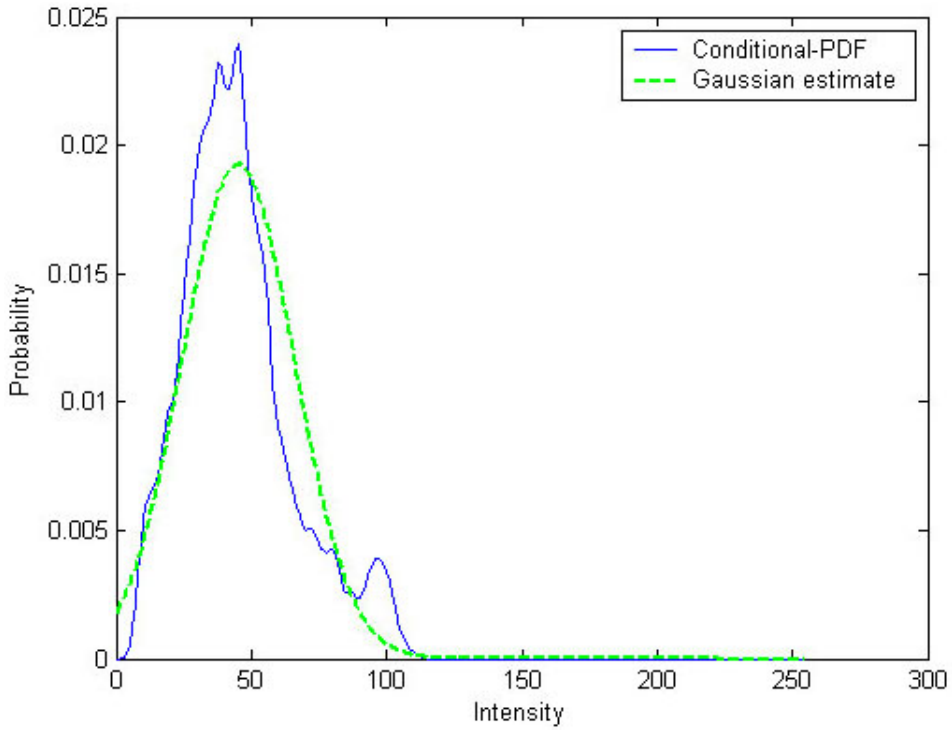

Figure 5.4: A conditional PDF, $P(E'|E, X = 35)$, and the estimated Gaussian distribution.

5.3 Comparing NMI estimation methods

To determine how the estimation error corresponds with registration results, a comparison will have to be to be made between the current paradigm of using Parzen density estimation and the new model using multivariate Gaussian estimation. First, to compare the differences in transformed coordinates, the deviation ΔT is found for the three directions, X, Y and Z according to Eq. (34), where T_P is the registered coordinates with Parzen density estimation, T_M is the registered coordinates with multivariate Gaussian estimation, and I is the index coordinates. ΔT is taken as the percentage magnitude difference in coordinates. The results for ΔT are obtained across 10 datasets for the different phases of registration and are shown in Figure 5.5.

$$\Delta T = \frac{\sum (T_P - T_M)^T (T_P - T_M)}{\sum (T_P - I)^T (T_P - I)} \times 100\% \qquad \ldots(34)$$

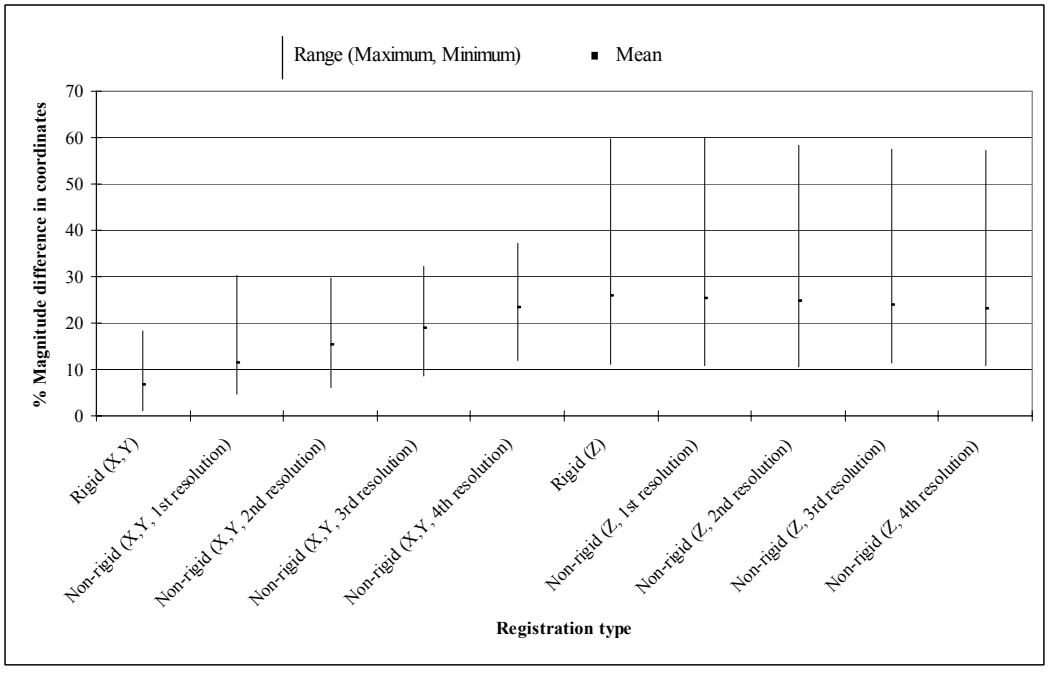

Figure 5.5: Magnitude difference of transformed coordinates comparing multivariate Gaussian estimation and Parzen density estimation. Measurements of in-plane coordinates (X, Y) were taken separately from through-plane coordinates (Z) because of the large statistical variation due to non-isotropic sampling in the through-plane direction.

The percentage ranges for in-plane transformation are smaller than those of through-plane, and the ranges and means increase with the progress of registration (from rigid to multi-resolution non-rigid). Through-plane transformation has a wider range of percentage difference, and its means and ranges do not vary significantly after rigid registration. The results indicate that the differences in transformation are relatively small (<60%), considering that the magnitude of transformed coordinates are mostly within a pixel width; thus we can consider the transformations to be relatively close.

However, the differences between transformed coordinates after non-rigid registration for scans with lesions were significant. Non-rigid registration using multivariate Gaussian estimation created some abnormal transformations when lesions were present, and this could only be clearly observed through visualization. Figure 5.6 compares three slices of in-plane meshes corresponding to CE-MRI slice in Figure 2.4, which shows a round benign lesion of approximately 12mm in diameter. Registration using multivariate Gaussian estimation gave an abnormal 'dome-shaped' mesh at the location of the lesion. This shows that the lesion had been compressed abnormally, which made it smaller and deformed despite regularization being applied. The reason optimization using multivariate Gaussian estimation resulted in an abnormal transformation was because the outlier distribution corresponding to lesions did not conform to the Gaussian shape as seen in Figure 5.4. Figure 5.7 demonstrates another instance of abnormal transformation that can be seen by comparing the difference images from the CE-MRI scans – here, the reduction in the lesion volume is unmistakable.

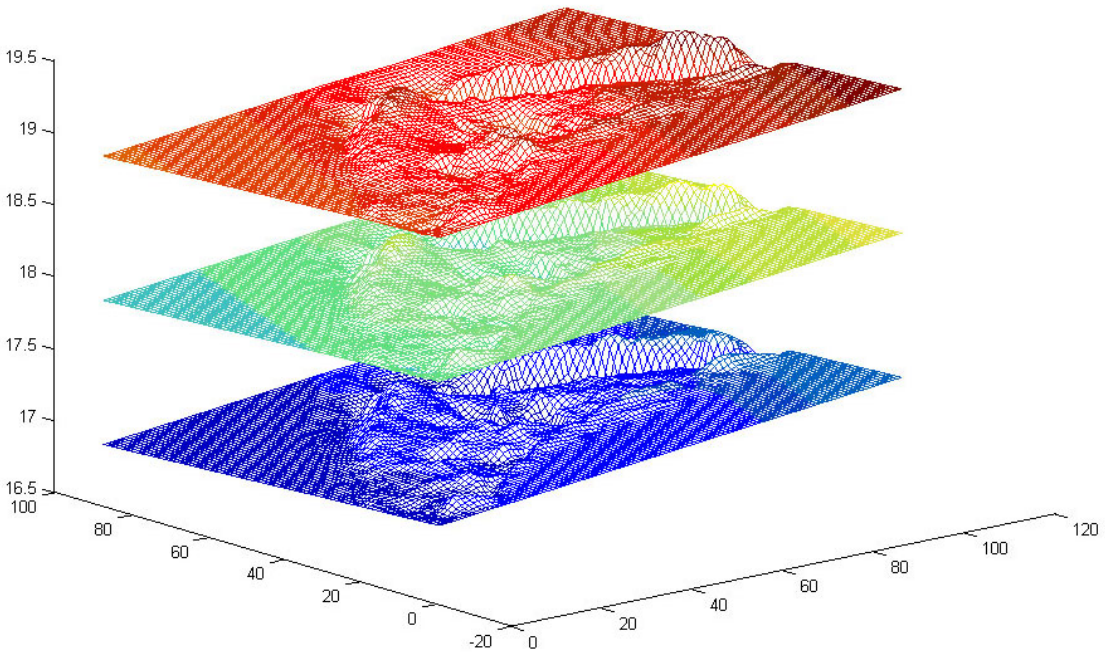

(a)

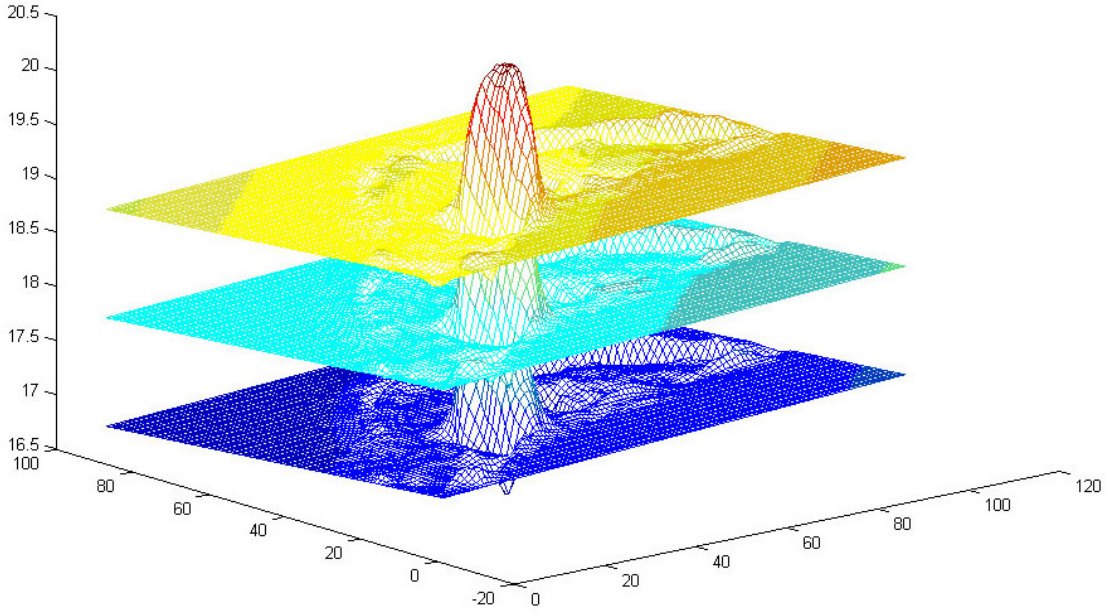

(b)

Figure 5.6: In-plane meshes after non-rigid registration using (a) Parzen window estimation, and (b) multivariate Gaussian estimation.

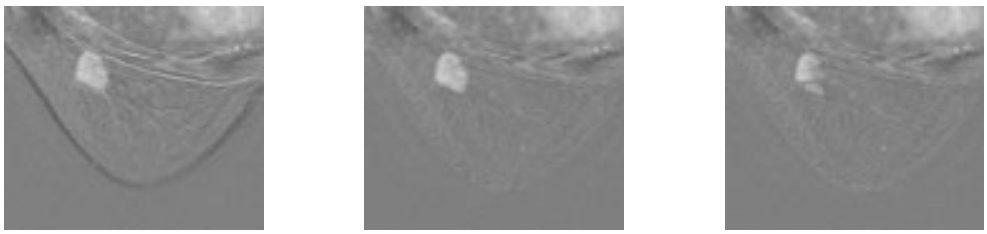

(a) (b) (c)

Figure 5.7: Observing effects of abnormal transformations on subtracted images. (a) Original subtracted image, (b) Subtracted image after non-rigid registration using Parzen density estimation, (c) Subtracted image after non-rigid registration using multivariate Gaussian estimation without segmenting lesions.

Before we present a method to prevent such abnormal transformations from happening, we want to compare the quality of registration. The indicators are NMI (found using Parzen density estimation), NNSD, CC and SSD. Normalized performance indicators K_{Rigid} and $K_{Non-rigid}$ of these indicators are used, substituting the symbol K with any of the four indicators. Positive values indicate better performance, and zero indicates equal performance. K_{Rigid} and $K_{Non-rigid}$ are defined as:

$$K_{Rigid} = \frac{\lambda_{Rigid} - \lambda_{Original}}{\zeta_{Rigid} - \zeta_{Original}} \times 100\% \quad \ldots(35)$$

$$K_{Non-rigid} = \frac{\lambda_{Non-rigid} - \lambda_{Rigid}}{\zeta_{Non-rigid} - \zeta_{Rigid}} \times 100\% \quad \ldots(36)$$

λ_{Rigid} and $\lambda_{Non-rigid}$ are the measurements (NMI, NNSD, CC or SSD) from registration using multivariate Gaussian estimation; ζ_{Rigid} and $\zeta_{Non-rigid}$ are the measurements from registration using Parzen density estimation; Results are found for 10 representative datasets and are shown in Table 5.1.

Table 5.1: Normalized measurements showing improvement of registration using multivariate Gaussian estimation over Parzen density estimation, shown as percentages (%).

Measurement	Registration	Max (%)	Min (%)	Average (%)
NMI	Rigid	17.3	-0.2	9.1
	Non-rigid	5.8	-1.2	1.9
NSSD	Rigid	6.2	-1.2	2.1
	Non-rigid	31	-5.1	6.9
CC	Rigid	5.3	-0.6	3.3
	Non-rigid	3.3	-1.0	1.1
SSD	Rigid	15.2	0.6	6.9
	Non-rigid	23.1	-1.1	9.2

Despite the apparent abnormality in its non-rigid transformation in scans with lesions, multivariate Gaussian estimation consistently yielded better registration quality than Parzen density estimation in all measurements. If registration using multivariate Gaussian estimation obtained better NMI values than Parzen density estimation, the registration using multivariate Gaussian estimation is more optimum than Parzen density estimation. Regularization is not the prime reason for better registration quality because this occurred for rigid registration as well.

The reason for this phenomenon can be attributed to the fact that the bell-shaped conditional PDFs of CE-MRI almost resembles Gaussians. Unlike multivariate Gaussian estimation, Parzen density estimation is not parameterized, so its search space is more prone to termination in local extrema. From here we can infer two things: (i) registration using Parzen density estimation can potentially create the abnormalities in Figure 5.6; and (ii) early termination may not give abnormal transformations, but it is by no means optimum. Therefore, non-rigid registration using Parzen density estimation terminates early, albeit compressing the lesion as observed before with

Rueckert's algorithm (Tanner *et al.*, 2001). The outlier distributions are a direct cause of the abnormalities, thus its effects cannot be assumed to be negligible.

5.4 Segmentation of hypervascularized regions

The other option to deal with outlier distributions is to exclude them from the optimization procedure. If segmenting away regions with outlier distributions can be done to make the conditional PDFs more Gaussian-like, the abnormalities are less likely to occur. If the outlier distributions are indeed the areas with lesions, then all that is needed is a lesion identification method. We will show if this is true.

The 3TP method is a clinically proven, sensitive way for identifying lesion regions (Kelcz *et al.*, 2000), and it also offers a way of varying non-rigid registration to the desired size of the lesions by varying the enhancement constants (κ_1 and κ_2). The 3TP derives its results from all sequences rather than only from the registered scan and the reference scan. Since it is a sensitive identification method, we propose to use the 3TP method for segmenting lesions for exclusion from non-rigid registration. As it is dependent on scans other than the reference and registered scans, it is a more sensible method than segmentation by thresholding outliers in the conditional PDFs.

We propose to apply 3TP segmentation only after rigid registration. This is due to the high unreliability of the 3TP method in the presence of registration artefacts. Particularly there are significant motion artefacts on the breast boundaries due to the high intensity gradient across breast boundaries, resulting in the conditional PDFs of non-registered images containing more outliers. So applying the 3TP segmentation method from the start (i.e., from a non-registered image) will result in such artefacts.

Table 5.2 shows the amount of reduction in the standard deviation of the estimated Gaussian with and without segmentation. Figure 5.8 compares the same conditional PDFs before and after rigid registration, showing how rigid registration reduces the standard deviation of the dominant distribution while making the outlier distribution more obvious. It had also been observed in previous experiments (Tan *et al.*, 2003A) that rigid registration phase accounted for majority of the motion artefacts removal in non-rigid registration. Table 5.3, on the other hand, compares the sum-of-squares probability error, which shows the amount of probability deviation from the estimated Gaussian. Prior to segmentation, the deviation from a true Gaussian distribution increased a little. This is because the reduction in the standard deviation due to rigid registration made the deviation due to the outliers more pronounced. Figure 5.8 also shows that after the lesions have been segmented (using $\kappa_1 = 60\%$ and $\kappa_2 = 0\%$), the outliers are gone, the standard deviation of the estimated Gaussian has been reduced, and the probability deviation has also been reduced despite a much smaller standard deviation. This shows that lesion segmentation using the 3TP method corresponds to the outlier distribution and that removal of the lesions after rigid registration result in a much better Gaussian fit.

Table 5.2: Comparing percentage reduction in standard deviation of conditional PDF across 10 datasets.

	Percentage reduction in standard deviation		
	Max	**Min**	**Mean**
Before segmentation (after rigid registration)	28.7	1.11	16
After segmentation (after rigid registration)	72.3	19.5	47

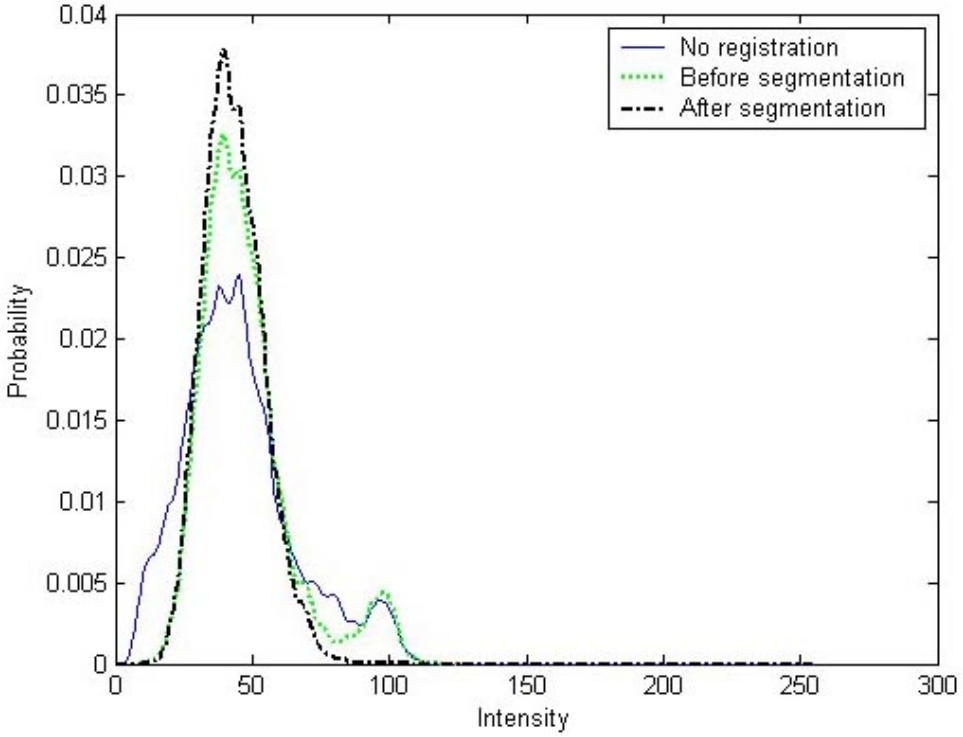

Figure 5.8: Conditional PDFs $P(E'|E, X = 35)$ comparing without registration, and before and after segmentation of lesion areas. Rigid registration was done before segmentation. After segmentation, the outliers at 100 were significantly reduced, and the PDF was more Gaussian like.

Table 5.3: Comparing the sum-of-squares probability error from estimated Gaussian distributions across 10 datasets.

	Sum-of-squares probability error		
	Max ($x10^{-4}$)	**Min ($x10^{-4}$)**	**Mean ($x10^{-4}$)**
No registration	47.3	9.21	20.2
Before segmentation (after rigid registration)	51.1	10.0	32.8
After segmentation (after rigid registration)	28.5	5.12	10.9
Before segmentation (after rigid registration)	28.7	1.11	16
After segmentation (after rigid registration)	72.3	19.5	47

Rigid transformations do not result in a change in volume, so the adverse effects of abnormal transformations will not occur during rigid registration. Multivariate Gaussian estimation may be used instead of Parzen density estimation in the rigid phase. Besides, there are only small differences in the transformed coordinates between rigid registration with Parzen density estimation and with multivariate Gaussian estimation (without segmentation, as shown in Figure 5.5). Another comparison also shows that rigid transformations after segmentation are closer to Parzen density estimation's transformations by (closer by 17% for in-plane, closer by 8.3% for through-plane). As multivariate Gaussian estimation is less computationally expensive, it is retained for rigid registration.

Next, we need to compare the transformed coordinates and to see if segmentation was successful in preventing abnormal transformations during non-registration. The transformed coordinates with segmentation are on average closer to Parzen density estimation than without segmentation (closer by 14% for in-plane, closer by 5.8% for through-plane). In addition, the abnormalities as previously seen in Figure 5.6(b) are not present (Figure 5.9).

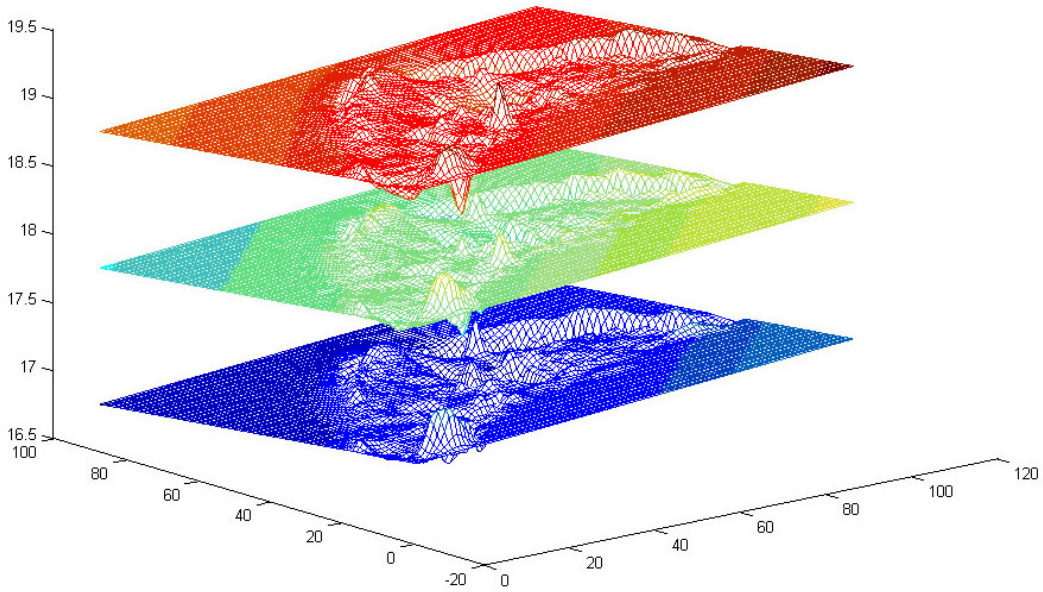

Figure 5.9: In-plane meshes after non-rigid registration using multivariate Gaussian estimation after segmentation.

The registration quality for non-rigid registration is compared in Table 5.4 using the normalized performance indicators from Eqs. (35) and (36). Multivariate Gaussian estimation with segmentation continues to outperform Parzen density estimation in NSSD (9.8%) and CC (24%), while the differences in NMI are small (-2.2%) on average. While SSD is significantly weaker (-11%), it should be noted that NSSD is a much better measurement than SSD because of the expected increase in intensity after the pre-contrast scan. In fact, this disparity shows that registration using multivariate Gaussian is more successful in targeting registration errors due to decrease in intensity. Though the improvements in CC are quite significant, it has been observed that CC measurements occasionally decreased after rigid registration. This is because CC cannot account for non-uniform intensity changes in CE-MRI.

Table 5.4: Normalized performance indicator measurements, $K_{Non-rigid}$ comparing results of non-rigid registration. Results obtained using multivariate Gaussian estimation with segmentation are normalized against results from Parzen density estimation.

Measurement	Max (%)	Min (%)	Average (%)
NMI	0.12	-8.1	-2.2
NSSD	18	-3.5	9.8
CC	56	1.0	24
SSD	-5.1	-21	-11

Registration using multivariate Gaussian estimation is thus comparable to using Parzen density estimation. We have shown that potential errors can occur with Parzen density estimation especially in reduction of lesion volume. Segmenting lesions using the 3TP method is successful in making a better fit between conditional PDFs the estimated Gaussians. Thus this new model of contrast enhancement is suitable for CE-MRI registration; multivariate Gaussian estimation will be used in the subsequent comparisons.

CHAPTER SIX

RESULTS AND DISCUSSION

The new registration paradigm adopted uses the new model of contrast enhancement. The results presented here use objective and subjective metrics of determining the quality of registration. Rigid and non-rigid registration results are compared thoroughly using quantitative and qualitative metrics. The efficiency of the new registration paradigm is also examined, before rounding up with a summary of the results and some discussion.

6.1 Comparing rigid against non-rigid registration

Quantitative results and visual assessments using a clinical reader were made using the new registration scheme. 22 CE-MRI datasets of varying scan sizes and pathology were processed, and each breast was analyzed separately, giving 42 breasts (2 patients underwent mastectomy previously). Among these, 20 are normal, and 22 have lesions (benign and malignant). A list of abnormalities is found in Table 5.5. Detailed assessments of cases of interest are also presented. A comparison of the efficiency of registration follows.

Table 6.1: The instances of abnormalities found from the pathology of the data.

Pathology	No. of cases
DCIS	5
Invasive lobular carcinoma	1
Axillary carcinoma	3
Malignant (others)	2
Benign fibroadenoma	4
Benign fibrosis post-treatment	1
Benign hemangioma	2
Benign sclerosing adenosis	1
Benign (others)	6
Implants	1

6.1.1 Quantitative results

The quantitative measurements used are NMI, NSSD, SSD, and CC. Contrary to the normalized performance indicators used in chapter 5, here we compare the measurements as percentages of their pre-registration measurements because the comparison is between rigid and non-rigid registration. Figure 6.1 shows this comparison between the two categories of normal breasts and breasts with lesions. Figure 6.2 provides the same information but shows how the measurements perform with respect to the sequence of the post-contrast scans.

Overall, registration quality improves with each phase of registration, indicating better alignment. The only exception to that is CC, which has an unexpected overall decrease with rigid registration, and a marginal increase after non-rigid registration (Figure 6.1). By observing the variation of CC with scan sequence (Figure 6.2), CC increases only during the 1st post-contrast scan; it is clear that the overall decrease of CC is because the strongest intensity increases occur between the 1st and 2nd post-contrast scans. CC

is only reliable for registering the 1st post-contrast scan using our protocol; thus it will not be used henceforth.

The magnitude and standard deviations of percentage changes are roughly the same for breasts with and without lesions. Registration quality for NMI and SSD are marginally higher in magnitude for breasts without lesions, and vice versa for NSSD. Thus NMI, SSD and NSSD achieved good generalization for breasts with and without lesions. Their consistencies also show that these three are good indicators of registration quality.

The results are also fairly constant across the sequences for NMI and SSD. The magnitudes for NSSD however increase with the sequence. This may be explained by the expected increase in intensity with sequence, which decreases absolute NSSD, hence increasing the percentage magnitudes.

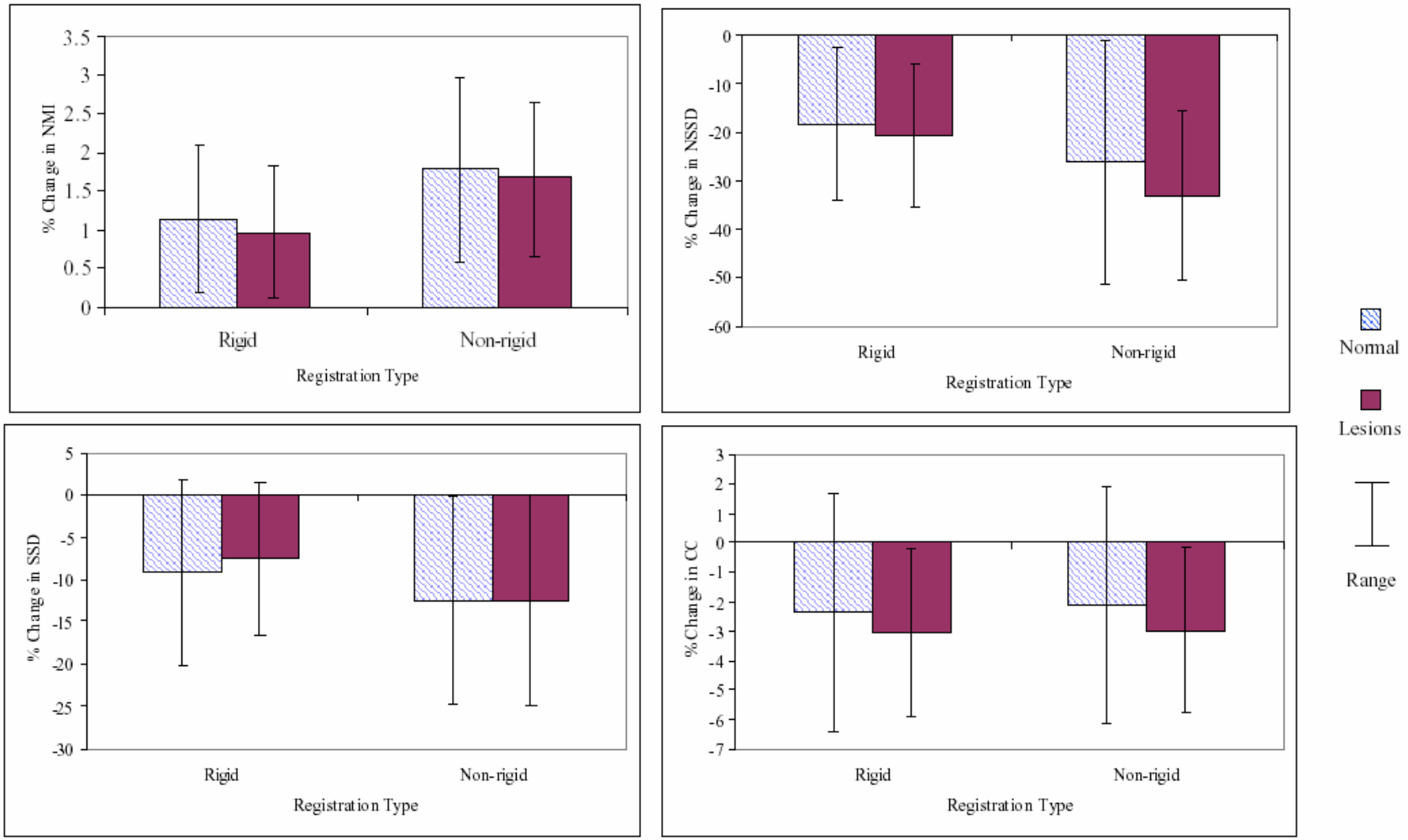

Figure 6.1: Percentage changes in quantitative measurements; in means (blocks) and standard deviation ranges (lines).

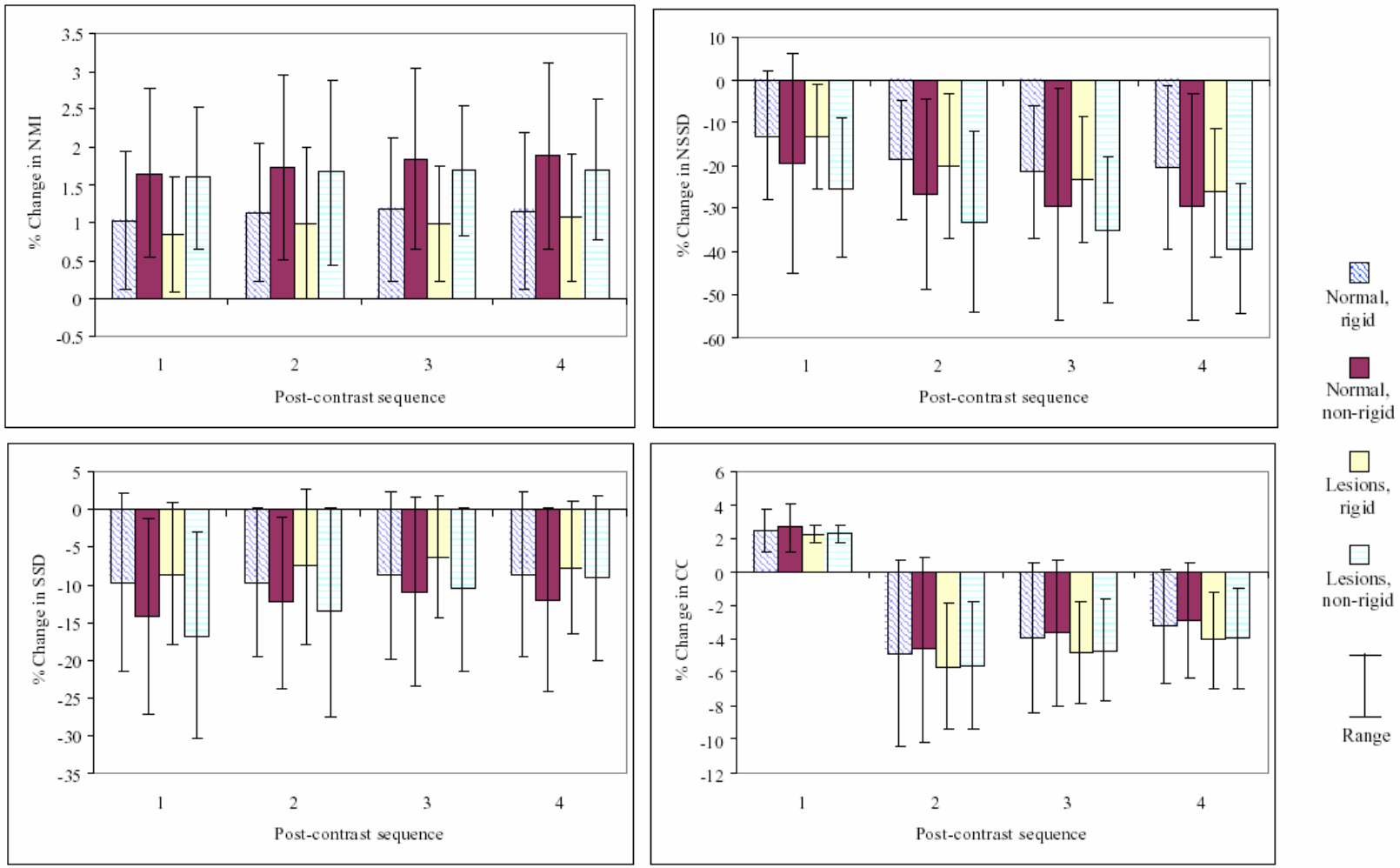

Figure 6.2: Percentage changes in quantitative measurements across sequences; in means (blocks) and standard deviation ranges (lines).

6.1.2 Visual assessments

A subjective scoring system is used to grade visual improvements resulting from registration. The assessments are divided into three categories. 'Skin line registration' considers the boundary of the breast; 'breast cone registration' considers the boundaries of the cone-shaped parenchyma; 'residual motion artefacts' is everything else in the breast of interest that has components of less significant image gradient as the earlier two categories. A 4-point score is used (see Table 6.2), of which the lowest score reflects the best perceived alignment. An expert radiologist in MRM is our clinical reader.

Table 6.2: 4-point score used by a clinical reader in visual assessments of registration results.

Feature	Score= 0	Score= 1	Score= 2	Score= 3
Skin line registration	Excellent	Good	Fair	Poor
Breast cone registration	Excellent	Good	Fair	Poor
Residual motion artefacts	Minimal	Slight	Moderate	Marked

Table 6.3 is a summary of the comparison of the visual assessments for normal breasts, and Table 6.4 is a summary for breasts with lesions. For normal breasts, rigid registration was always at least as good as pre-registration, and non-rigid registration was always at least as good as pre-registration. The same was observed for rigid registration of breasts with lesions; non-rigid registration was worse than rigid registration 9.1% of the time for skin line registration, but had more instances of better scores. In the cases with worse results, non-rigid registration had the same scores as pre-registration. Thus, non-rigid registration in general improved the visual quality of the images.

Skin line and breast cone registration tends to be better than residual motion artefacts registration for both types of breast. This is because the boundaries of the skin and the breast cones have stronger image gradient. Visually, it is also easier to observe improvements in alignment in regions with stronger image gradient.

Table 6.3: Visual assessments for 20 normal breasts using a clinical reader based on a 4-point score; comparing skin line registration (SKIN), breast cone registration (CONE), and residual motion artefacts (MOTION).

Registration	Comparison	SKIN	CONE	MOTION
Rigid vs. no registration	Better (%)	50.0	70.0	20.0
	Same (%)	50.0	30.0	80.0
	Worse (%)	0.0	0.0	0.0
Non-rigid vs. rigid	Better(%)	50.0	40.0	25.0
	Same (%)	50.0	60.0	75.0
	Worse (%)	0.0	0.0	0.0

Table 6.4: Visual assessments for 22 breasts with lesions using a clinical reader based on a 4-point score; comparing skin line registration (SKIN), breast cone registration (CONE), and residual motion artefacts (MOTION).

Registration	Comparison	SKIN	CONE	MOTION
Rigid vs. no registration	Better (%)	68.2	54.5	18.2
	Same (%)	31.8	45.5	81.8
	Worse (%)	0.0	0.0	0.0
Non-rigid vs. rigid	Better (%)	72.7	31.8	18.2
	Same (%)	18.2	68.2	81.8
	Worse (%)	9.1	0.0	0.0

6.1.3 Cases of interest

Figure 6.3 compares a slice from a breast with DCIS. Rigid registration accounted for majority of artefact removal, especially around at the boundaries. The clinical reader analysis concurs, that rigid and non-rigid registration improved skin-line registration, while only rigid registration improved breast cone registration. Changes in quantitative measurements are consistent with visual observations – in NMI, 1.8% and 2.7% for rigid and non-rigid respectively; in SSD, -13.0% and 16.0%; and in NSSD, -38.2% and -44.8%. When 3TP analysis was done, the images displayed distinct regions of malignancy when the enhancement parameters were set as $\kappa_1 = 90\%, \kappa_2 = 50\%$. It was found that majority of malignant regions were better characterized by high initial enhancements ($\kappa_1 > 150\%$) than with a fast wash-out. This was because the scans used spanned 3-5 minutes postinjection to focus on initial enhancements; no scans were taken during the 6-10 minutes postinjection period when wash-out is usually observed.

Figure 6.4 compares a slice taken from a breast with benign fibroadenoma. In this case, rigid and non-rigid registration resulted in visual improvements in skin-line registration and breast-cone registration. Analysis using 3TP with $\kappa_1 = 90\%, \kappa_2 = 30\%$ erroneously displayed more internal regions with malignancy at pre-registration than after non-rigid registration, and more 3TP-detected lesions along the skin. The changes in measurements were consistent in NMI (2.0%, 4.4%), in SSD (-23.4%, -36.0%), and in NSSD (-14.2%, -48.9%).

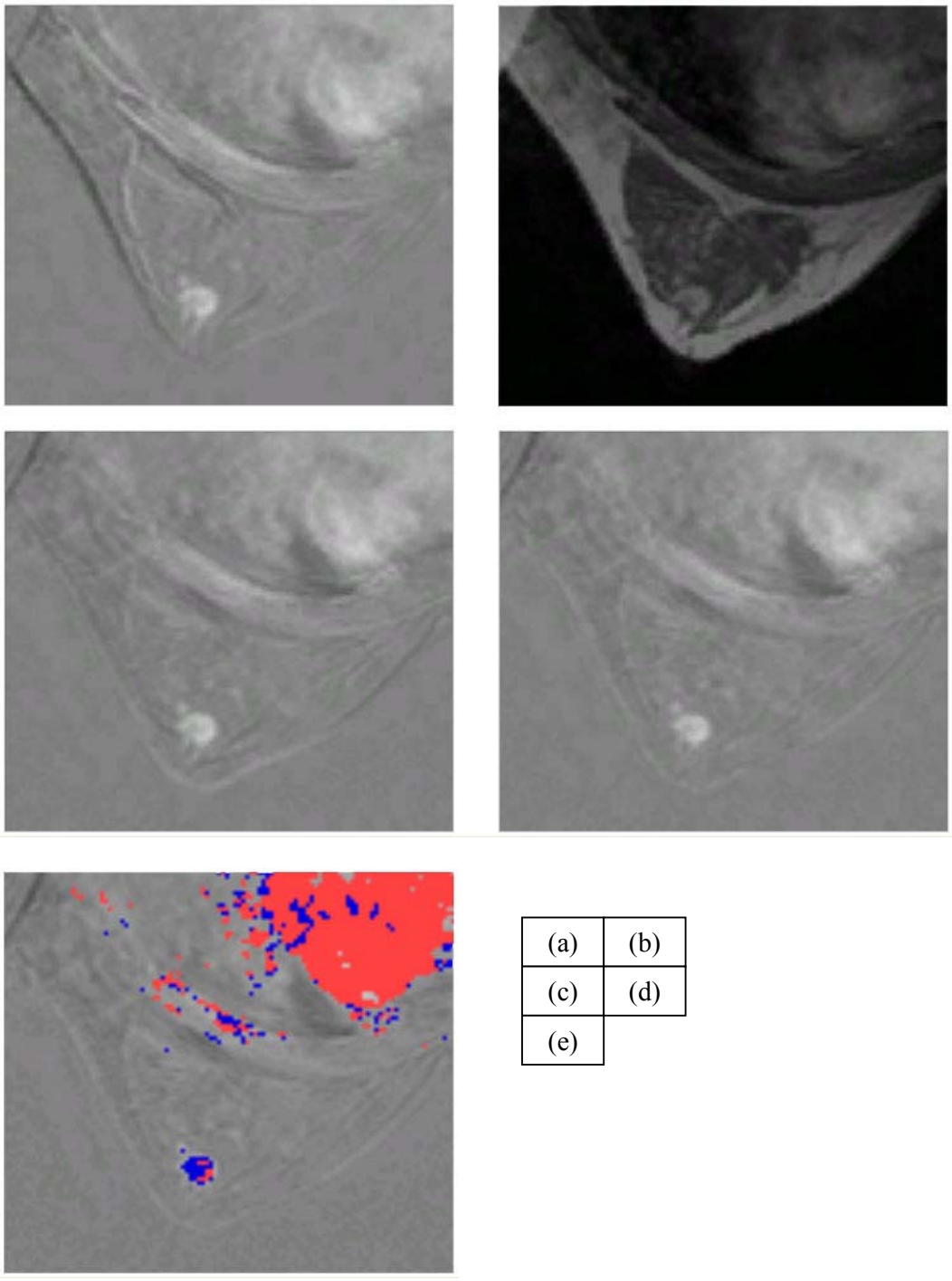

(a)	(b)
(c)	(d)
(e)	

Figure 6.3: Comparing registration for a case with DCIS. (a) Pre-registration subtraction image; (b) Pre-registration original image; (c) Rigid registration subtraction image; (d) Non-rigid registration subtraction image; (e) Non-rigid registration with 3TP ($\kappa_1 = 90\%, \kappa_2 = 50\%$)

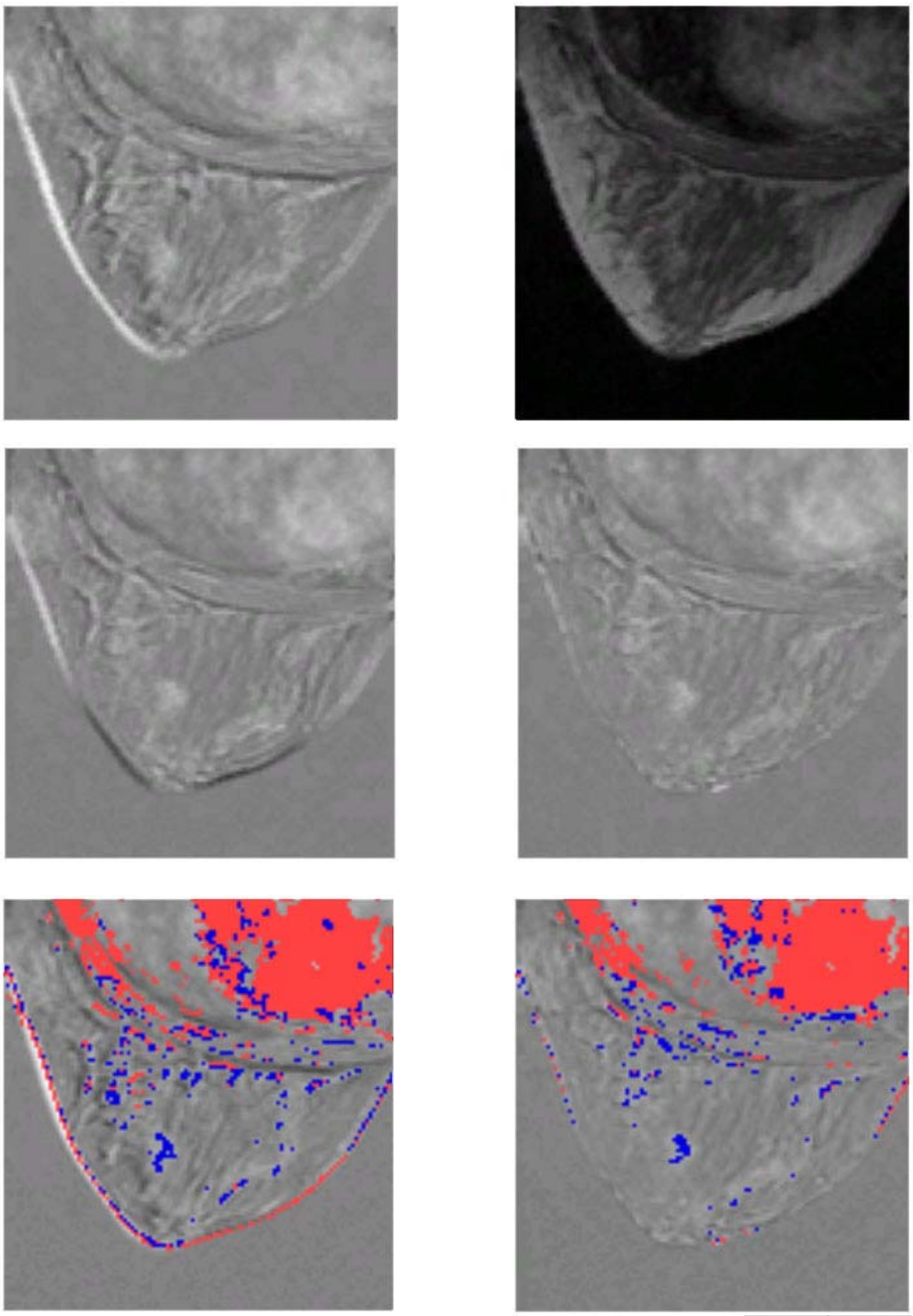

Figure 6.4: Comparing registration for a case with benign fibroadenoma. (a) Pre-registration subtraction image; (b) Pre-registration original image; (c) Rigid registration subtraction image; (d) Non-rigid registration subtraction image; (e) Pre-registration with 3TP ($\kappa_1 = 90\%, \kappa_2 = 30\%$); (f) Non-rigid registration with 3TP ($\kappa_1 = 90\%, \kappa_2 = 30\%$)

(a)	(b)
(c)	(d)
(e)	(f)

6.1.4 Efficiency

The time taken for registration is compared. Figure 6.5 shows that both phases are approximately linear to the size of the images, where the time taken is that of the entire dataset (typically four runs of registration for four post-contrast volumes). Rigid registration takes about 0.225ms per voxel; non-rigid registration takes about 0.670ms per voxel. The largest registered image (3.1 million voxels) took less than an hour. The reason for this linearity is the multivariate Gaussian estimation. Registration using the Parzen density estimation took 0.4 to 3.8 times longer for rigid registration, and 2.6 to 7.5 times longer for non-rigid registration. Thus, the new registration scheme is predictably fast, and is feasible to use in a clinical environment where high throughput may be needed.

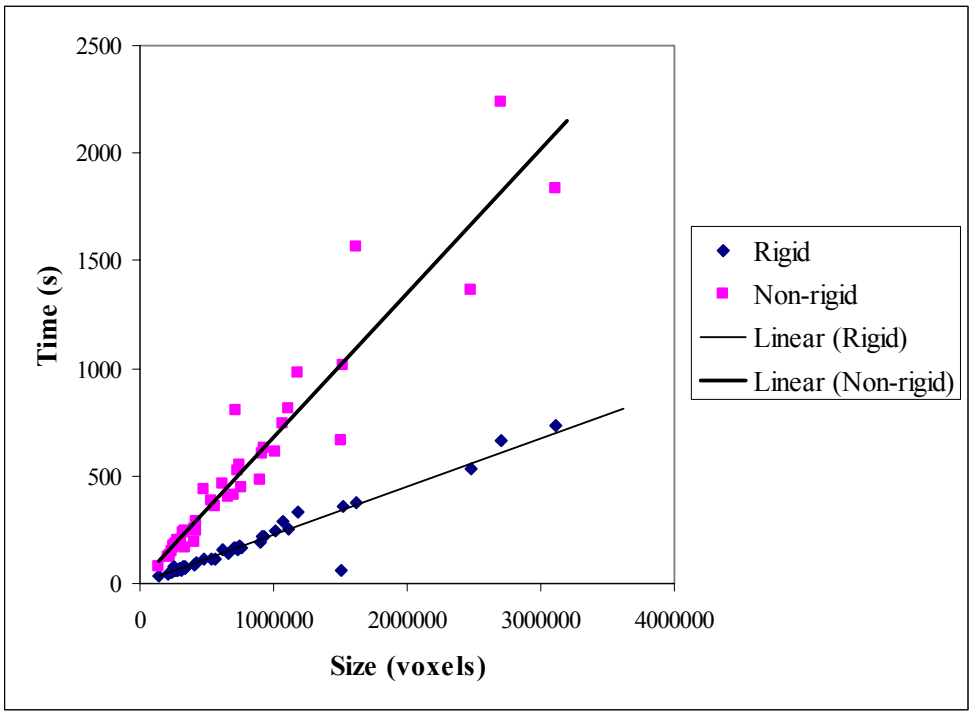

Figure 6.5: Comparing time taken for the rigid and non-rigid phases of registration against dataset size.

6.2 Summary of results and discussion

The new model of contrast enhancement proposed has been shown to be theoretically consistent and was verified experimentally. Multivariate Gaussian estimation has been shown to be much more efficient than Parzen density estimation, and has given comparable measurements in terms of quality of registration. Without segmentation, non-rigid registration may result in abnormal transformations at regions with hypervascularity, which is the failing of current registration paradigm. Applying segmentation solves this problem, while retaining registration quality. The improvements in visual quality are matched in quantitative measurements in small population study of breasts with varying conditions. It has been found that rigid and non-rigid registration almost always have had at least equal visual quality in the skin line, in the breast cone, and in other residual regions. Registration is needed to reflect accurate detection using enhancement analysis methods like 3TP.

It should be noted that the theoretical parameters for the 3TP method were not suited to analyzing our studies. However, 3TP remained sensitive to lesion detection in general without distinguishing malignancy, which is useful to the segmentation of lesions for non-rigid registration with the new model. Another aspect of the 3TP method that has not been investigated is the variation of enhancement parameters in segmentation. By decreasing (increasing) the sensitivity of the parameters to lesions, the degrees of freedom of transformations can be increased (decreased). When implemented interactively or adaptively, registration can be customized to the sizes of lesions expected, to balance between lesion obliteration and motion artefact reduction.

Also, “ghosting” aliasing artefacts are made more obvious by the subtraction process, whether registered or unregistered, and has only been partially reduced by the use of rigid or non-rigid registration. Such gross motion artefacts are not usually troubling from a diagnostic clinical reader’s perspective as they are visually obvious and usually can be ignored. However, they may be important for automated analysis algorithms. A separate approach will be necessary to remove this specific artefact, probably during the initial preprocessing phase.

CHAPTER SEVEN

CONCLUSION

7.1 Summary

This thesis has presented a scheme for the non-rigid registration of MRM. This scheme improves on currently available registration paradigms, the best of which uses global and local motion modeling and optimizes NMI. We have proposed a new contrast enhancement model that parameterizes optimization of NMI using multivariate Gaussian estimation. This assumes that the intensity mappings due to motion artefacts and contrast enhancement can be mainly modeled as Gaussians. We have shown that the assumptions of multivariate Gaussian estimation can be met if outliers in the estimated Gaussians can be segmented out from registration; we have also shown that the current NMI registration paradigm is much slower, and can potentially result in erroneous registration. Comparable registration results have been achieved when the new contrast enhancement model was applied, leading us to adopt this new registration paradigm.

The effects of the new registration scheme have been analyzed using quantitative measurements and qualitative visual assessments by an experienced clinical reader. The measurements show that non-rigid registration is better than rigid registration, and rigid registration surpasses pre-registration images. Visual analysis has revealed that non-rigid registration was at least as good as pre-registration images, and was better than pre-registration most of the time. The time required for the new scheme has also

been found to be linear to the image size used for registration – this shows that registration can be a manageable process especially when high throughput is required.

In examining the results using the 3TP method, we have demonstrated that accurate registration is required to produce the correct analysis. Thus, a fast and improved registration scheme that can enable accurate clinical analysis of CE-MRI has been proposed. With accurate clinical analysis, CE-MRI will become a more reliable tool for breast cancer detection.

7.2 Future Work

In our work, we have used the 3TP method for voxel by voxel analysis. As demonstrated in section 6.1.3, the theoretical parameters for 3TP may not be suitable for the CE-MRI protocol used in our experiments and in NUH, as these rapidly acquired sequences occur over the first 3 to 5 minutes after contrast injection; most studies using 3TP obtain a later time point (6 to 10 minutes postinjection) for lesion washout analysis. More research can be done on creating a more reliable method for determining malignancy.

Jacobs *et al.*, (2003) used a novel multi-parametric method to analyze CE-MRI. This required analyzing both T1- and T2-weighted images, which is not done traditionally and in this thesis. The registration scheme proposed in this project may also be applied to multimodality registration between T1- and T2-weighted images.

The incorporation of the 3TP method into registration can also be investigated further. By varying the parameters of 3TP when segmenting lesions in non-rigid registration,

the user can interactively change the desired degree of registration to find a balance between artefact removal and lesion preservation.

The registration scoring process has shown that gross intra-sequence motion which caused “ghosting” of the breast due to macroscopic motion by the patient was not eliminated by the registration process. However, the unregistered raw images can be readily adjusted to visually minimize or even eliminate the appearance of such “ghosts”. Paradoxically then, the registration process has made such large-scale motion artefacts more visible, not less. Preprocessing of the initial images by filtering may be able to further minimize these macroscopic “ghost artefacts.

REFERENCES

[Azar *et al.*, 2002] F.S. Azar, D.N. Metaxas, & M.D. Schnall, "Methods for modeling and predicting mechanical deformations of the breast under external perturbations", in Med. Image Anal. 6: 1-27, 2002.

[Baum *et al.*, 2002] F. Baum, U. Fischer, R. Vosshenrich & E. Grabbe, "Classification of hypervascularized lesions in CE MR imaging of the breast", Eur. Radiol. 12:1087-1092, 2002.

[Behrenbruch *et al.*, 2003] C.P. Behrenbruch, K. Marias, P.A. Armitage, M. Yam, N. Moore, R.E. English, J. Clarke, & M. Brady, "Fusion of contrast-enhanced breast MR and mammographic imaging data", in Med. Image Anal. 7: 311-340, 2003.

[Buckley *et al.*, 1994] D. Buckley, R. Kerslake, S. Blackband, & A. Horsman, "Quantitative analysis of multi-slice Gd-DTPA enhanced dynamic MR images using a automated simplex minimization procedure", Magnetic Resonance Medicine, 32. 646-651, 1994.

[Chia *et al.*, 2000] K.S. Chia, A. Seow, H.P. Lee & K. Shanmugaratnam, "Cancer Incidence in Singapore 1993-1997" in Singapore: Singapore Cancer Registry, 2000.

[Chia *et al.*, 2002] K.S. Chia, J.J.M. Lee, J.L.L. Wong, W. Gao, H.P. Lee & K. Shanmugaratnam, "Cancer Incidence in Singapore, 1998-1999" in Ann. Acad. Med Singapore 2002; 31:745-50, 2002.

[Choi *et al.*, 2002] B.G. Choi, H.H. Kim, E.N. Kim, B. Kim, J.Y. Han, S. Yoo & S.H. Park, "New subtraction algorithms for evaluation of lesions on dynamic contrast-enhanced MR mammography", Eur. Radiol. 12:3018:3022, 2002.

[Collignon *et al.*, 1995]A. Collignon, F. Maes, D. Vandermeulen, P. Suetens & G. Marchal, "Automated multi-modality image registration based on information theory",

in Bizais, Y., Barillot, C. and di Paola, R. (eds), Proc. XIVth Int. Con& Information Processing in Medical Imaging, Computational Imaging and Vision, Vol 3, pp. 263-274, Be de Berder, France. Kluwer Academic Publishers, Dordrecht, 1995.

[Le Cun *et al.*, 1990] Y. Le Cun, J. S. Denker, and S. Solla, "Optimal brain damage" Advances in Neural Information Processing Systems 2:598-605, 1990.

[Degani *et al.*, 1997] H. Degani, V. Gusis, D. Weisntein, S. Fields & S. Strano, "Mapping pathophysiological features of breast tumors by MRI at high spatial resolution", in Nature Medicine, 3:780-782, 1997.

[Fahlman, 1998] S.E. Fahlman, "An empirical study of learning speed in back-propagation networks", CMU-CS-88-162, September 1988.

[Fischer *et al.*, 1999] H. Fischer, M. Otte, C. Ehritt-Braun, J. Laubenberger, J. Hennig, "Local Elastic Matching and Pattern Recognition in MR Mammography", Imaging Syst Technol, 10, 199–206, 1999.

[Fornefett *et al.*, 2001] M. Fornefett, K. Rohr, H. S. Stiehl, "Radial basis functions with compact support for elastic registration of medical images", Image and Vision Computing 19, pp 87-96, 2001.

[Furman-Haran *et al.*, 2001] E. Furman-Haran, D. Grobgeld, F. Kelcz, H. Degani, "Critical Role of Spatial Resolution in Dynamic Contrast-Enhanced Breast MRI", in J. Magnetic Resonance Imaging, 13:862:867, 2001.

[Hassibi *et al.*, 1993] B. Hassibi, D.G. Stork, and G.J. Wolff, "Optimal brain surgeon and General Network Pruning", in Proceeding IEEE International Conference on Neural Networks, San Francisco, 1: 293-299, 1993.

[Hayton *et al.*, 1997] P. Hayton, M. Brady, L. Tarassenko, and N. Moore, "Analysis of dynamic MR breast images using a model of contrast enhancement" *Med. Image Anal.* vol. 1 no. 3, pp. 207-224, 1997.

[Hayton *et al.*, 1999] P.M. Hayton, M. Brady, S.M. Smith, N. Moore, "A non-rigid registration algorithm for dynamic breast MR images", Artificial Intelligence 114, pp 125-156, 1999.

[Heywang-Köbrunner & Beck, 1996] S. H. Heywang-Köbrunner & R. Beck, "Contrast-Enhanced MRI of the Breast", 2nd Edition, Springer, 1996.

[Horn & Schunck, 1981] B.K.P. Horn & B.G. Schunck, "Determining optical flow", Artificial Intelligence 17:185–203, 1981.

[Ikeda *et al.*, 2001] D.M. Ikeda, N.M. Hylton, K. Kinkel, M.G. Hochman, C.K. Kuhl, W.A. Kaiser, J.C. Weinreb, S.F. Smazal, H. Degani, P. Viehweg, J. Barclay & M.D. Schnall, "Development, standardization, and testing of a lexicon for reporting contrast-enhanced breast magnetic resonance imaging studies", in J. Magnetic Resonance Imaging, 13:889-895, 2001.

[Jacobs *et al.*, 2003] M.A. Jacobs, P.B. Barker, D.A. Bluemke, C. Maranto, C. Arnold, E.H. Herskovits & Z. Bhujwalla, "Benign and malignant breast lesions: diagnosis with multiparametric MR imaging", in Radiology, pp.225-232, 2003.

[Kelcz *et al.*, 2000] F. Kelcz, E. Furman-Haran, D. Grobgeld, H. Degani, "Clinical testing of the 3tp method for breast MRI diagnosis", Second International Congress On MR-Mammography, Institute of Diagnostic and Interventional Radiology, Friedrich Schiller University Jena, Germany, September 21-23, 2000.

[Kumar *et al.*, 1996] R. Kumar, J.C. Asmuth, K. Hanna, J. Bergen, C. Hulka, D.B. Kopans, R. Weisskoff, and R. Moore, "Application of 3D registration for detecting lesions in magnetic resonance breast scans" *Proc. SPIE Medical Imaging 1996: Image Processing* vol. 2710, pp. 646-656, 1996.

[Leventon & Crimson, 1998] M.E. Leventon & W.E.L. Crimson, "Multi-modal Volume Registration Using Joint Intensity Distributions", in Medical Image

Computing and Computer-Assisted Intervention - MICCAI'98, ed. by W.M. Wells, A. Colchester, S. Delp, Cambridge, MA, Springer LNCS 1496, pp. 1057, 1998.

[Likar & Pernuš , 2001] B. Likar, F. Pernuš, "A hierarchical approach to elastic registration based on mutual information", Image and Vision Computing 19, pages 33–44, 2001.

[Loew & Carranza, 1998] M. H. Loew, C. E. Rodriguez-Carranza, "Technical issues in multimodality medical image registration", 11th IEEE Symposium on Computer-Based Medical Systems, pp. 2-7, June 12 - 14, 1998.

[Maes *et al.*, 1997] F. Maes, A. Collignon, D. Vandermeulen, G. Marchal, P. Suetens, "Multimodality Image Registration by Maximization of Mutual Information", IEEE Transactions on Medical Imaging, vol. 16, no. 2, April 1997

[Maes *et al.*, 1999] F. Maes, D. Vandermeulen, P. Suetens, "Comparative evaluation of multiresolution optimization strategies for multimodality image registration by maximization of mutual information", Medical Image Analysis (1999) vol. 3, no. 4, pp 373-386

[Maintz & Viergever, 1998] J. B. A. Maintz, M. A. Viergever, "A survey of medical image registration", Medical Image Analysis (1998), vol. 2, no. 1, pp 1-36.

[Maintz *et al.*, 2001] J. B. A. Maintz, P. A. van del Elsen, & M. A. Viergever, "3D Multimodality medical image registration using morphological tools", Image and Vision Computing 19:53-62, 2001.

[Nelder & Mead, 1965] J.A. Nelder & R. Mead, "A Simplex Method for Function Minimization" in *Computer Journal* 7:308-313, 1965.

[Pluim *et al.*, 2000] J. P.W. Pluim, J. B. A. Maintz, and M. A. Viergever, "Interpolation artefacts in mutual information-based image registration," Comput. Vision Image Understanding, vol. 77, no. 2, pp. 211–232, 2000.

[Rainer & Aldo, 2000] K.D.M. Rainer, von W. Aldo, "Parallel Implementation of a MR-Mammography Matching Algorithm" Proceedings of the 13th IEEE Symposium on Computer-based Medical Systems (CBMS'00), June 2000 in Houston, Texas, USA.

[Reichenbach *et al.*, 2002] J.R. Reichenbach, J. Hopfe, M E. Bellemann, W.A. Kaiser, "Development and validation of an algorithm for registration of serial 3D MR breast data sets", Magnetic Resonance Materials in Physics, Biology and Medicine, pages 249-258, 5 February 2002.

[Riedmiller, 1994] M. Riedmiller, "Rprop – Description and Implementation Details" Institut für Logik, Komplexität and Deduktionssyteme, Technical Report, Januaray 1994.

[Rohde *et al.*, 2003] G.K. Rohde, A. Aldroubi, B.M. Dawant, "The adaptive bases algorithm for intensity-based nonrigid image registration", in IEEE Transactions on Medical Imaging, Vol. 22, No. 11, pp. 1470-1479, November 2003.

[Rouet *et al.*, 2000] J.-M. Rouet, J.-J. Jacq, C. Roux, "Genetic Algorithms for a Robust 3-D MR-CT Registration", IEEE Transactions on IT in Biomedicine, vol. 4, no. 2, June 2000.

[Rueckert *et al.*, 1999] D. Rueckert, L.I. Sonada, C. Hayes, D.L.G. Hill, M.O. Leach, D.J. Hawkes, "Non-rigid Registration Using Free-form Deformations: Application to Breast MR Images", IEEE Transactions in Medical Imaging, vol. 18, no. 8, August 1999.

[Schnabel *et al.*, 2001] J. A. Schnabel, D. Rueckert, M. Quist, J. M. Blackall, A. D. Castellano-Smith, T. Hartkens, G. M. Penney, W. A. Hall, H. Liu, C. L. Truwit, F. A. Gerritsen, D. L. G. Hill, D. J. Hawkes, "A Generic Framework for Non-rigid Registration Based on Non-uniform Multi-level Free-form Deformation", MICCAI 2001: 573-581.

[Schnabel *et al.*, 2003] J.A. Schnabel, C. Tanner, A. Castellano Smith, A. Degenhard, C. Hayes, M.O. Leach, D.R. Hose, D.L.G. Hill, D.J. Hawkes, "Validation of Non-rigid Registration using Finite Element Methods: Application to Breast MR Images", IEEE Transactions in Medical Imaging, vol. 22, no. 2, February 2003.

[Studholme *et al.*, 1999] C. Studholme, D. L. G. Hill, and D. J. Hawkes, "An overlap invariant entropy measure of 3D medical image alignment," Pattern Recognit., vol. 32, no. 1, pp. 71–86, 1999.

[Szeliski & Coughlan, 1994] R. Szeliski, J. Coughlan, "Hierarchical Spline-based Image Registration", Technical Report 94/1, Digital Equipment Corporation, Cambridge Research Lab, April 1994.

[Tan *et al.*, 2003A] E. T. Tan, C.H. Yan, S. H. Ong, S. C. Wang, "An adaptive scheme for non-rigid registration in MRI mammography", World Congress on Medical Physics and Biomedical Engineering 2003 – Poster Presentation, 24-29 August 2003, Sydney, Australia.

[Tan *et al.*, 2003B] E. T. Tan, C. H. Yan, S. H. Ong, S. C. Wang, "Elastic alignment of contrast-enhanced dynamic MRI mammography", 7th NUS-NUH Annual Scientific Meeting – New Frontiers in Medicine, P-124, 2-3 October 2003, Singapore.

[Tollenaere, 1990] T. Tollenaere, "SuperSAB: Fast adaptive backpropagation with good scaling properties", in Neural Networks vol 3., pp.561-573, 1990.

[van Engeland *et al.*, 2003] S. van Engeland, P. Snoeren, J. Hendriks & N. Karssemeijer, "A comparison of methods for mammogram registration", in IEEE Trans. On Medical Imaging, Vol. 22, No. 11, pp. 1436-1444, November 2003.

[Viola, 1995] P. A. Viola, "Alignment by maximization of mutual information", M.I.T. A.I. Technical Report No. 1548, Ph.D Thesis, June 1995.

[Tanner *et al.*, 2001] C. Tanner, A. Degenhard, J.A. Schnabel, A. Castellano Smith, C. Hayes, L.L. Sonoda, M.O. Leach, D.R. Hose, D.L.G. Hill & D.J. Hawkes, "A Method for the Comparison of Biomechanical Breast Models", In IEEE Workshop on Mathematical Methods in Biomedical Image Analysis, pp. 11–18. 2001.

[Wang, 1999] S. C. Wang, "Magnetic resonance imaging of the breast", in Gynecologic Imaging, John C. Anderson, Churchill Livingstone, pp.703-748, 1999.

[Wang, 2003] S. C. Wang, "The Singapore National Breast Screening Programme: Principles and Implementation", in Ann. Acad. Med. Singapore 32:466-76, 2003.

[Wells *et al.*, 1996] W. M. Wells, P. Viola, H. Atsumi, S. Nakajima, "Multi-modal Volume Registration by Maximization of Mutual Information", in Medical Image Analysis, 1(1):35-51, 1996.

[Woods *et al.*, 1992] R.P. Woods, S.R. Cherry & J.C. Mazziotta, "Rapid automated algorithm for aligning and reslicing PET images", J Comput Assist Tomogr 16, 620–633, 1992.

[Zuo *et al.*, 1996] C.S. Zuo, A. P. Jiang, B.L. Buff, T.G. Mahon & T.Z. Wong, "Automatic motion correction for breast MR imaging" *Radiology* vol. 198, pp. 903-906, 1996.